Understanding the Role of Cellular Dynamics in MDCKII Domes Formation

A Thesis

submitted to

Indian Institute of Science Education and Research Pune in partial fulfilment of the requirements for the BS-MS Dual Degree Programme

by

Kishan Kurpati Raghavendra

Indian Institute of Science Education and Research Pune

Dr. Homi Bhabha Road,

Pashan, Pune 411008, INDIA.

Date: April, 2026

Under the guidance of

Supervisor: Dr. Stefano Villa,

Max Planck Institute for Dynamics and Self-Organization

From May 2025 to Mar 2026

INDIAN INSTITUTE OF SCIENCE EDUCATION AND RESEARCH PUNE

Certificate

This is to certify that this dissertation entitled 'Understanding the role of Cellular Dynamics in MDCKII Domes formation' towards the partial fulfilment of the BS-MS dual degree programme at the Indian Institute of Science Education and Research, Pune represents work carried out by Kishan Kurpati Raghavendra at The Max Planck Institute for Dynamics and Self-Organization in Göttingen, Germany under the supervision of Dr. Stefano Villa, Group leader, Laboratory for Fluid Physics Pattern Formation and Biocomplexity, during the academic year 2025-2026.

Committee:

Guide: Dr. Stefano Villa

TAC expert: Dr. Richa Rikhy

This thesis is dedicated to my friends and colleagues in Göttingen, without whom this work would not have been possible.

My friends—Sidharth Das, Somdatta Naskar, Nandana V. Uday, Keerthana C. J., Robab Jahangir, and Marina Lorenzo—along with my colleagues, Vahid Nasirimarekani, Katharina Gunkel, and Angela Gremmel, as well as many others whom I cannot name here, have made my time and work in Göttingen an unforgettable experience.

Declaration

I hereby declare that the matter embodied in the report entitled 'Understanding the role of Cellular Dynamics in MDCKII Domes formation' are the results of the work carried out by me at the Laboratory for Fluid Physics Pattern Formation and Biocomplexity, The Max Planck Institute for Dynamics and Self-Organization in Göttingen, Germany, under the supervision of Dr. Stefano Villa, and the same has not been submitted elsewhere for any other degree. Wherever others contribute, every effort is made to indicate this clearly, with due reference to the literature and acknowledgement of collaborative research and discussions.

Kishan Kurpati Raghavendra

20211273

Table of Contents

List of Figures

Abstract

Epithelial monolayers serve fundamental physiological roles in development, homeostasis, and disease; yet how collective cell dynamics and substrate mechanics coordinate to drive three-dimensional morphogenesis remains poorly understood. Here, we investigate how substrate mechanics and pharmacological modulation of cell motility and contractility influence monolayer dynamics, dome formation kinetics, and cell adhesion in MDCKII epithelial cells.

Using epifluorescence and spinning disk confocal microscopy, we tracked monolayer dynamics and dome formation on glass, PDMS, and uniform or micropatterned protein coatings. Quantitative analysis of velocity fields revealed a transient motility peak 55-67 hours post-seeding. HGF increased peak velocities in a dose-dependent manner, while blebbistatin suppressed motility and contractility without altering adhesion strength. Blebbistatin-treated cells formed smaller domes that collapsed gradually rather than suddenly, with rapid dome turnover and shorter lifetimes. In contrast, PDMS—which reduces adhesion while increasing motility—produced larger domes with collapse dynamics similar to controls. Confocal imaging revealed that dome collapse involves transient loss of actin stress fibers in dome cells, which are then pulled outward by contractile neighbors before repolarizing and migrating back—a recovery abolished by blebbistatin. Centrifugation-based adhesion assays quantified substrate-specific detachment thresholds.

These findings reveal that monolayer motility and dome kinetics are governed by interplay between actomyosin contractility, cell motility, and substrate adhesion, with implications for understanding epithelial morphogenesis, tissue mechanics, and biomaterial design.

Acknowledgments

I am immensely thankful to my supervisor and guide, Dr. Stefano Villa, for his continuous and consistent feedback and input on all my experiments. I also thank him for several of the analyses credited to him in this thesis. I am grateful to Sidharth Das, a friend and labmate, for his valuable feedback. I am deeply grateful to the lab technicians—Ms. Katharina Gunkel, Ms. Maren Stella Müller, and Ms. Lara Ständer—for taking care of the cells and the lab, and for their weekly assistance with my experiments.

I acknowledge the Machine Shop at the Max Planck Institute for Dynamics and Self-Organization (MPI-DS), and particularly Mr. Andy Heil, for helping us build our custom cell adhesion assay setup. I am thankful to Dr. Mišo Mitkovski and Mr. Heiko Röhse for their expertise and technical assistance at the Facility for Light Microscopy at the Max Planck Institute for Multidisciplinary Sciences (MPI-NAT), City Campus, for multiphoton and confocal microscopy. I also thank the Facility for Light Microscopy for access to software tools such as Arivis and Nikon NIS Elements for analysis.

I would also like to thank Ms. Angela Gremmel at MPI-DS for helping with all the bureaucracy in Germany and MPI-DS. I thank MPI-DS and the Indian Institute of Science Education and Research (IISER), Pune, for the opportunity to pursue this master's thesis, and MPI-DS for financial support for my stay. I acknowledge the receipt of the Kishore Vaigyanik Protsahan Yojana (KVPY) fellowship.

Contributions

Contributor name	Contributor role
Dr. Villa	Conceptualization Ideas
Kishan and Dr. Villa	Methodology
Dr. Villa and Kishan	Software
Kishan	Validation
Dr. Villa	Formal analysis
Kishan and Dr. Villa	Investigation
Dr. Villa and Prof. Bodenschatz	Resources
Kishan	Data Curation
Kishan	Writing - original draft preparation
Kishan and Dr. Stefano Villa	Writing - review and editing
Kishan	Visualization
Dr. Villa	Supervision
Dr. Villa	Project administration
Prof. Bodenschatz	Funding acquisition

This contributor syntax is based on the Journal of Cell Science CRediT Taxonomy.

Generative AI Usage

Generative AI tools were used solely for proofreading and minor language refinement of selected passages in this thesis. Specifically, DeepSeek R1 Distill Llama 70B hosted on the GWDG server was utilized for this purpose. The model's outputs were reviewed and, where necessary, modified by the author. No substantive content generation or analysis was performed using generative AI. Data sent to the model, including prompts and message contents, are not stored on GWDG systems (https://docs.hpc.gwdg.de/services/ai-services/chat-ai/models/index.html).

1. Introduction

1.1 Epithelial tissue

Epithelial tissue is one of the most widespread and important tissue types in the body. It forms the outer surfaces of many organs, creating dense, stable layers that provide protection. These layers also serve as interfaces for biological functions (Clemente-Suárez *et al.*, 2023). This tissue is responsible for the functioning and maintenance of several organ systems, including the gastrointestinal tract, urogenital tract, and endocrine system (Clemente-Suárez *et al.*, 2023).

Epithelial tissues are characterized by a polarized organization, with distinct apical and basolateral domains that perform specialized functions. This layered polarity is maintained by tight junctions, adherens junctions, desmosomes, and gap junctions. These structures provide mechanical strength and facilitate intercellular communication, allowing the maintenance of polarity that is critical for normal physiological functioning (Brückner and Janshoff, 2018).

Epithelial cells are always exposed to physical forces, both in normal body function and in disease. For example, epithelial cells lining the intestine are pushed and stretched by muscle movements during peristalsis (Atarashi *et al.*, 2017; Jing *et al.*, 2020). In disease conditions such as chronic inflammation or tumor growth in the gut and lungs, constant pressure can build up in the whole organ. This pressure also affects the epithelial layer that lines these organs (Winter *et al.*, 2010; Jing *et al.*, 2020; Khusnurrokhman and Wati, 2022).

Lung alveolar and tubular epithelial cells undergo continuous expansion and relaxation during breathing, and this pressure is further altered in states such as asthma (Tschumperlin and Margulies, 1999; Brightling *et al.*, 2012). Therefore, understanding the response and mutual feedback between epithelial cell behavior and mechanical stress is important for a wide range of topics concerning physiological functioning.

1.2 Dome Formation in Epithelial Monolayers

Inside the body, epithelial cell layers form distinct fluid compartments maintained by transepithelial transport of ions and water, which generates osmotic gradients that drive water flow and separate different compartments, such as the lumen of the gut, the ducts of glands, and the external environment (Spring, 2011; Seifter and Chang, 2017; Ishida-Ishihara *et al.*, 2020). When cultured *in vitro* on solid, flat substrates they form confluent monolayers.

A widely used model in biomedical research since 1958 (Madin and DarbyJr, 1958) are MDCKII cells, which are epithelial cells derived and immortalized from canine kidney nephrons (Madin and DarbyJr, 1958).

Monolayers in culture perform apical-to-basal solute transport. At confluency*, in vitro* on non-permeable flat surfaces, this process increases ion concentration on the basal side, generating an osmotic gradient that drives fluid flux (Ishida-Ishihara *et al.*, 2020). The resulting pressure induces localized detachment and dome formation. Domes are self-organizing, hemispheric three-dimensional and fluid-filled structures that develop beneath a confluent monolayer. Domes are observed in various cell lines, including lung alveolar cells, mammary gland cells (Lever, 1979b; Wirl *et al.*, 1995), and kidney epithelial cells (Choudhury *et al.*, 2022). They grow as the fluid-filled lumen expands and eventually rupture and collapse back into the monolayer.

Foundational research in the 1970s established dome formation as a hallmark of differentiated, transporting epithelia. Lever's work demonstrated that domes arose from active ion transport rather than proliferation. In MDCK and mammary epithelial models, dome frequency was markedly increased by diverse reagents that are inducers of erythroid differentiation in Friend erythroleukemia cells (e.g., DMSO, butyrate, cAMP-elevating agents). Crucially, dome collapse upon ouabain addition directly implicated Na+/K+-ATPase-driven transport in their maintenance (Lever, 1979a).

By the 1990s, dome formation was leveraged as a quantitative readout for epithelial differentiation and toxicology. Automated image analysis systems were developed to

measure dome number and total area. Studies demonstrated that dome metrics could be suppressed in a dose-dependent manner by nephrotoxic agents like cisplatin, establishing the model's utility for cytotoxicity screening (Cotovio *et al.*, 1993)

A key mechanistic controversy emerged regarding whether domes were primarily sites of specialized active transport or simply areas of weak substrate adhesion. This was addressed by Sugahara et al. (Sugahara *et al.*, 1984) who used a vibrating microelectrode to detect extracellular current flow out of domes in alveolar and MDCK cells. This current was amiloride- and ouabain-sensitive and sodium-dependent and was uniform throughout the monolayer, leading to the conclusion that sodium is transported across the entire monolayer and leaks back apically, preferentially through domes. These findings suggest that domes arise in areas of reduced adhesion, likely driven by intrinsic intercellular variability.

A study by Saw et al. (Saw *et al.*, 2017) revealed that epithelial monolayers exhibit liquid crystal-like properties, with cells displaying long-range orientational order and anisotropy. These tissues develop topological defects, specifically comet-shaped +1/2 defects. At the head of these +1/2 defects, highly localized compressive stress is generated, which serves as a primary trigger for cell extrusion. Given that these defects create zones of mechanical instability, one might make the hypothesis that regions presenting such defects could similarly locally trigger large-scale detachment characteristic of dome formation.

Another candidate that could determine the location and kinetics of dome formation is cell dynamics. In epithelial monolayers, continuous cell movement generates mechanical stresses; because the tissue is dynamically reorganizing rather than static, these motions may locally concentrate stress and trigger dome initiation. As this possibility has not been systematically examined, we aim to test this hypothesis and investigate the relationship between cell dynamics and dome formation in greater detail. Understanding how cell dynamics interact with mechanical pressure to shape three-dimensional structures is important for revealing how epithelial tissues organize, remodel, and respond to physical forces during development and disease.

The dome system provides a useful framework to study these processes, as dome formation emerges from the combined effects of cell motility, substrate adhesion, and pressure generated by transepithelial fluid flux. Domes represent an intermediate level of

complexity: unlike conventional two-dimensional cultures, they capture three-dimensional mechanical interactions, yet they remain far simpler and more tractable than highly complex systems such as whole embryos. Because domes consist of a monolayer of a single cell type, individual cells can be tracked over time while still preserving key aspects of three-dimensional organization. Together, these features make domes a powerful platform for investigating epithelial mechanobiology.

In a study by Latorre et al., cells forming part of domes were observed to increase their area dramatically, experiencing areal strains of up to 1000% (Latorre *et al.*, 2018). In their study, fibronectin was micropatterned with holes that lacked the protein, creating defined areas of low adhesion that favored detachment, thus imposing dome formation in pre-determined spaces. They found that as cells stretch, the actin cortex spreads thinner. This allows some cells to enter a "superstretched" state while their neighbors remain relaxed. Intermediate filaments prevent unlimited expansion in these superstretched cells, creating a bistable system where cells exist in either a relaxed or superstretched state. While impactful, the system studied (3D domes pinned on a micropatterned surface) is artificially constrained and lacks physiological relevance for understanding the natural interplay between cell dynamics and mechanical pressure. Very little is known about the mechanisms underlying spontaneous dome formation, raising fundamental questions about where domes initiate and how these sites are determined.

1.3 Preliminary Observations and Study Aims

We aim to extend this inquiry through empirical tests that provide statistically significant information on the relationship between cell dynamics and dome formation kinetics. For this, we use the well-established MDCK-II cell system.

Preliminary data collected in our group showed that dome formation kinetics differs on Polydimethylsiloxane (PDMS) versus plastic substrates. Specifically, the evolution in the number and size of domes varied.

We know that PDMS surfaces reduces cell adhesion compared to tissue culture plastic because of its low surface energy and hydrophobicity (Patrito *et al.*, 2007; Hsieh *et al.*, 2011).

The v_{rms} , a measure of internal cell agitation (refer section 2.6.1), was found higher for cells on PDMS after reaching confluency around 45 hours post-seeding (Figure 1.1C). The number of domes on PDMS peaked around 50 hours, then slightly reduced and plateaued. At longer timescales, dome numbers were consistently lower than on plastic (Figure 1.1A). The mean dome area was also higher on PDMS from around 45 hours post-seeding (Figure 1.1B).

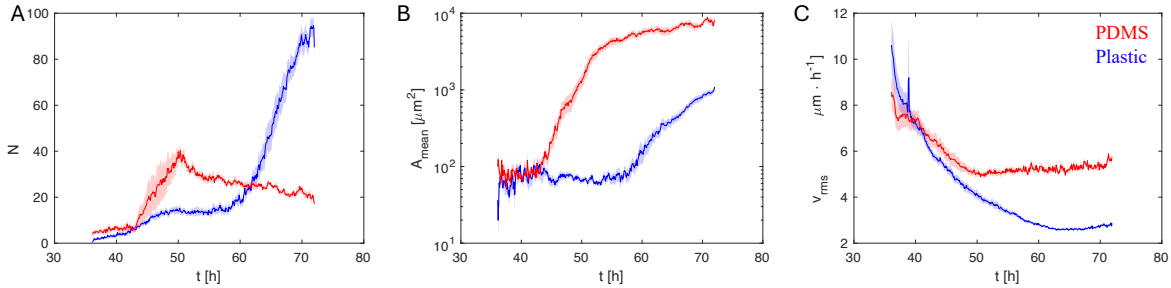

Figure 1.1: Varying dome and cell dynamics for different substrates*. Trends for cells grown on plastic are in blue; PDMS trends are in red. (A) Number of domes. (B) Average dome area. (C) Cell v_{rms} over time. T=0 is the seeding time. (Credits: Dr. Stefano Villa)*

This data indicates that cellular properties such as motility and substrate adhesion are key determinants of dome formation and organization. The use of PDMS simultaneously alters both adhesion and motility, making it difficult to distinguish their individual contributions. Therefore, we aim to dissect these factors independently and examine their specific roles in greater detail. Our study seeks to systematically investigate the interrelationship between cell adhesion, cell motility, and dome formation using a quantitative and statistically robust approach.

1.4 Extracellular Matrix and Cytoskeletal Mechanics

The extracellular matrix (ECM) is a highly organized structure consisting of several glycoproteins and proteoglycans. Collagens and fibronectin form a major part of the ECM. The most abundant proteins are members of the collagen family (Gelse, 2003),which are widely distributed in connective tissues. Fibronectin is another important part of the ECM that facilitates cell adhesion (Höök *et al.*, 1977; Chiquet *et al.*, 1979). It is a glycoprotein shed by fibroblasts present in all connective tissues (Vaheri *et al.*, 1976).

The ECM provides essential biochemical and mechanical cues to epithelial cells. It consists of two main components: the basal membrane directly under the epithelium, and a looser network called the interstitial matrix beneath it. This interaction is altered during disease stages such as tumor formation and cancer (Candiello *et al.*, 2007; Kozyrina *et al.*, 2020). In our experiments, we use collagen and fibronectin to facilitate cell adherence to substrates.

Cellular contraction is powered by actin and myosin. Non-muscle myosin II motors exert forces on filamentous actin through ATP hydrolysis. The primary architecture of filamentous actin exists in two main forms. The first is stress fibers, which have three subtypes: transverse arcs, dorsal stress fibers, and ventral stress fibers. These are connected to focal adhesions at zero, one and two points, respectively (Hotulainen and Lappalainen, 2006).The second form is a contractile actin cortex, where actin forms a cage-like mesh in the cell cortex, tethered to the membrane by ezrin (Charras *et al.*, 2006).

Focal adhesions connect to the ECM. Contractions in the linked actomyosin filaments generate traction, enabling cell movement. Furthermore, ablating a single stress fiber in a compliant medium causes viscoelastic retraction of the cut ends, compensatory ECM relaxation, and cell shape change (Kumar *et al.*, 2006). This demonstrates that tension is stored and released within these bundles, coupling them directly to cell mechanics. Therefore, understanding actin filament structure and patterns under pressure is crucial for understanding epithelial mechanical properties.

1.5 Experimental Approach

To study the effect of differing cell motilities, we will use pharmacological tools to specifically modulate cell motility on a single substrate, making it possible to dissect the individual contribution of motility from that of adhesion and examine their specific roles in dome formation.

Using epifluorescence and brightfield imaging, we will capture both dome dynamics and cell motility. For a closer view of dome growth and collapse, we will use a spinning disk

confocal microscope with dyes for nuclei and actin. Furthermore, we aim to measure relative cell-substrate adhesion strength under various conditions. This will be done using fluid shear to detach cells, either in a microfluidic device or with a centrifugal adhesion assay.

1.6 Impact

Understanding these fundamental mechanical interactions has an interest that goes beyond *in vitro* settings, as it has profound implications for how we interpret epithelial tissue behavior. From embryonic development to adult tissue homeostasis and disease states, epithelial cells experience various mechanical forces. During animal development, embryos are organized in epithelial layers from the blastocyst stage through the final stages of organ formation. Based on studies on *Drosophila* embryos, the monolayered cell sheet that undergoes gastrulation share several features with epithelial monolayers such as epithelial cell junctions (Eichenberger-Glinz, 1979) and an apico-basally polarized membrane (Shiel and Caplan, 1995; Müller and Wieschaus, 1996). Gastrulation is a crucial stage in early embryonic development where a single-layered ball of cells (blastula) reorganizes into a three-layered structure (gastrula), involving – in addition to chemical signaling and cellular differentiation – stresses and dynamics driving extensive tissue folding (Müller and Wieschaus, 1996). As developmental biologist Lewis Wolpert stated, "It is not birth, marriage or death, but gastrulation which is truly the most important time in your life."

In this framework, our project aims to decode and model one contributing factor—how mechanical forces interact with cellular dynamics and behavior within epithelial tissues. We seek to address this question under relatively simple experimental conditions, where imaging is accessible and three-dimensional organization can be studied within a monolayer of tractable cells.

2. Materials and Methods

2.1 Cells and Culture

MDCKII WT cells were purchased from Sigma (00062107-1VL) and received gratefully from Prof. Jahnsoff's lab. Cells from Prof Jahnsoff's lab were used for all experiments unless mentioned otherwise.
Cells are grown at 37°C with 5% CO_2 in incubators starting from a seeding density of 3.1 X 10^4 cells/cm^2 (in such a density so that cells reach confluency in 48 hours).
Recombinant Human HGF (HEK293 Derived) was acquired from Peprotech.
InSolution Blebbistatin was acquired from EMD Millipore

2.2 Preparation of coatings

2.2.1 Preparation of PDMS Coating

Sylgard 184 elastomer base was mixed with Sylgard 184 elastomer curing agent at a 10:1 ratio. To remove air bubbles formed during mixing, the mixture was placed in a vacuum desiccator for 30 minutes. It was then poured onto the desired surface to achieve a complete coating of the surface and incubated at 70°C for two hours to cure.

To enhance hydrophilicity and promote the adsorption of subsequent coatings (collagen), the PDMS surface was treated with oxygen plasma and stabilized with APTES using the following procedure adopted from (Siddique *et al.*, 2017): The PDMS surface was first washed three times with Dulbecco's phosphate-buffered saline (PBS, Sigma-Aldrich) and allowed to dry for 15 minutes. The dried surface was then treated with oxygen plasma for 2 minutes (0.5 mbar O_2, 50% power) in a plasma cleaner. Immediately following plasma treatment, a 2% (v/v) APTES solution prepared in acetone was applied to the surface and incubated for 15 minutes. Finally, the surface was washed three times with PBS and coated with collagen as described in Section 2.2.2.

2.2.2 Preparation of collagen coating

The surface was first washed three times with PBS. FITC-conjugated type-I collagen from bovine skin was purchased from Sigma-Aldrich. Collagen FITC was used to validate the coating of collagen. Collagen from calf skin (Sigma) was also used for the rest of the experiments. A stock concentration of 1 mg/mL was diluted to 4 µg/mL using 10 mM acetic acid. The diluted collagen solution was applied at 0.5 mL per well in a 24-well plate or 1 mL per 35 mm dish (IBIDI µ-Dish 35 mm, high) to fully cover the surface. After allowing

the collagen to settle for one hour, the surface was washed three times with PBS. The lid of the coated surface was then sealed with parafilm and stored at 4°C for up to one week before use.

2.2.3 Fabrication of SU-8 Cylinders on a Silicon Wafer

A mask was designed using KLayout, consisting of circles with a radius of 100 μm, spaced 600 μm apart center-to-center. The design file was sent to a commercial vendor for mask printing.

All subsequent fabrication steps were performed in a cleanroom environment to prevent contamination from dust particles. First, a silicon wafer was placed on a 200°C hot plate for at least two minutes and then cleaned using an air gun.

A measured volume of SU-8 photoresist was applied to the wafer, which was then spun at 500 RPM for 30 seconds. The wafer underwent a soft bake on a hot plate: one minute at 65°C, followed by several minutes at 95°C (the duration determined by the desired final cylinder height), and finally one more minute at 65°C.

The wafer was then transferred to a mask aligner (Cloé UV Kub3). The chrome photomask, mounted on a glass plate and wiped with acetone, was loaded with the chrome side facing down. Using the aligner's software, the exposure was configured with the following parameters: constant dose mode, vacuum contact, a separation distance of 80 μm, with mask and substrate thickness excluded. The exposure dose was calculated using a standard formula based on the target thickness.

After visually inspecting and repositioning the wafer to optimize alignment, exposure was initiated. Following exposure, the wafer was developed to remove unexposed photoresist, rinsed with isopropanol, and then hard-baked using the same temperature sequence as the soft bake. Finally, the wafer was rinsed with isopropanol, and the thickness of the fabricated cylinders was verified using a profilometer.

2.2.4 Preparation of Soft PDMS with Beads and Micro-patterned Fibronectin

This protocol was adopted from (Latorre *et al.*, 2018). Silicones CY52-276A and CY52-276B (Dow-Corning) were mixed at a 1:1 ratio. The mixture was degassed in a vacuum desiccator for one minute and then spin-coated onto IBIDI 35 mm dishes. A volume of 350 µL was applied, followed by spinning at 250 RPM for 6 seconds and then 1500 RPM for 60 seconds on a Chemat KW4A spin coater. The coated dishes were cured at 70°C for two hours.

The cured soft PDMS surface was treated with oxygen plasma for 2 minutes (0.5 mbar O_2, 50% power) in a plasma cleaner. It was subsequently treated with 5% (v/v) 3-aminopropyltriethoxysilane (APTES; Sigma-Aldrich) in absolute ethanol for three minutes, rinsed three times with 96% ethanol, and allowed to dry.

A PDMS stamp was fabricated by creating SU-8 cylinders (100 µm diameter) on a silicon wafer and coating them with a layer of PDMS as described in Section 2.2.1. This stamp was incubated in fibronectin (40 µg/mL) for one hour at room temperature, allowed to dry, and immediately placed in conformal contact with a polyvinyl alcohol (PVA; Sigma-Aldrich) membrane. A 100 g weight was placed on the stamp for 20 minutes. The patterned side of the PVA membrane was then placed face-down onto the bead-treated soft PDMS gel and incubated for one hour.

A 0.2% (w/v) solution of Pluronic F-127(Sigma) was added to the gel to dissolve the PVA membrane while passivating non-patterned areas, and the assembly was incubated overnight at 4°C. The following day, the gel was washed three times with PBS to remove PVA and excess Pluronic, then incubated with warm culture medium at 37°C for 30 minutes.

Finally, the medium was removed and a 200 µL droplet containing 300,000 cells was added to the patterned region. Cells were allowed to adhere for 50 minutes in an incubator. The surface was then gently washed to remove unattached cells, fresh medium was added, and the culture was maintained for 72 hours before use, with a medium refresh after 48 hours.

2.2.5 Seeding cells on polycarbonate filters

To separate the basal and apical compartments of the monolayer, cells were grown on Nunc™ Polycarbonate Cell Culture Inserts in Multi-Well Plates (Techno Fisher Scientific; pore size 0.4 µm). Cells were seeded at a density of 3.1×10^4 cells/cm², with 2 mL of medium added above the cells and 2 mL below the cells as shown in figure 2.1. The medium was changed on day 3 and then collected and changed again on day 5 and day 7. The fluorescence of the collected medium was recorded using an epifluorescence microscope (see Section 2.3.1).

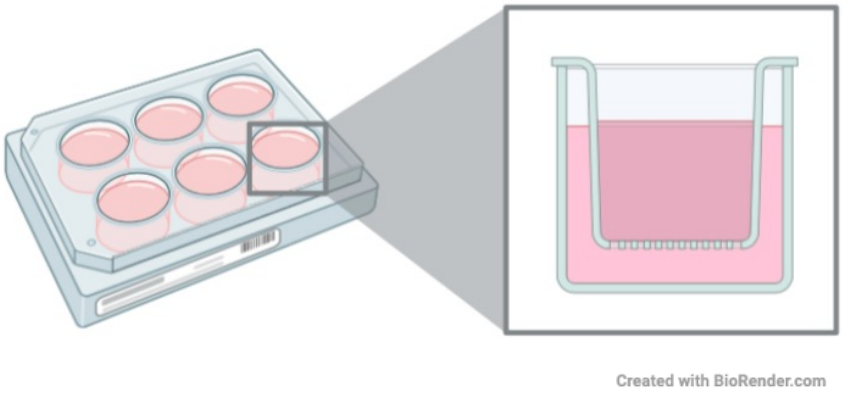

Figure 2.1:Schematic representation of the polycarbonate filters: *The illustration depicsts how the polycarbonate filters were placed in 6 well plates for culturing cells*

2.3 Live cell imaging

2.3.1 Epifluorescence imaging

To observe monolayer dynamics and dome formation, the medium was changed on the third day after seeding, and blebbistatin (InSolution) or HGF (PeproTech) was added at the desired concentrations. An Olympus IX83 inverted microscope equipped with a 10× objective and a Pecon climate chamber was used to acquire brightfield and epifluorescence images. For each condition, at least four fields of view per well were recorded, with two wells per condition in a 24-well plate. Time-lapse imaging was performed at 5-minute intervals for live observation of monolayer behavior.

2.3.1.1 Live/Dead Assay

The Live/Dead assay distinguishes viable cells from dead cells using two fluorescent dyes. Live cells possess intracellular esterase activity that converts non-fluorescent calcein AM into green-fluorescent calcein (ex/em ~495 nm/~515 nm), which is well retained within

intact cells. Dead cells with damaged membranes take up EthD-1, which undergoes a 40-fold fluorescence enhancement upon binding to nucleic acids, producing bright red fluorescence (ex/em ~495 nm/~635 nm). EthD-1 is excluded by the intact membranes of live cells (LIVE/DEAD™ Viability/Cytotoxicity Kit (Invitrogen) manual).

For this assay, the LIVE/DEAD™ Viability/Cytotoxicity Kit (Invitrogen) was used with 2 mM EthD-1 and 2 µM calcein AM, applied one hour before imaging. Acquisition was once every 12 hours (see section 2.3.1 for acquisition settings). However, since calcein is unsuitable for long-term imaging and its signal leaks out of cells over time, only the death assay was performed.

Dead cell counting was carried out using TrackMate in Fiji. A diameter setting of 16.9 µm was applied. The sensitivity threshold was selected by analyzing the software's histogram, which displays a characteristic bimodal distribution, with the first peak corresponding to the noise and the second peak corresponding to the nuclei. To avoid erroneous segmentation of background noise, a threshold value was chosen immediately after the first peak (= 35 in our case). For each sample, the total number of dead cells was quantified across two wells covering the entire field of view. The mean and standard deviation were calculated and divided by the maximum number of cells that could theoretically fit within the microscope's field of view, yielding the percentage of dead cells.

2.3.2 Confocal imaging

Confocal imaging was done at the Light microscopy facility at the Max Planck Institute for Multidisciplinary Sciences. To visualize singular domes in greater detail, we used a Nikon Ti2 Spinning Disk Confocal inverted microscope for imaging at 40X fitted with an Okolab incubator. Recording began on the fourth day after seeding. SiR Actin (Spirochrome) was used at a concentration of 100 nM with 5 µM Verapamil. SPY-595 (Spirochrome) was used at a 1000X dilution to visualize nuclei. All stains were introduced by dissolving them in 1 mL of fresh medium and replacing the old medium at least one hour before imaging began. After selecting the desired fields of view in the associated Nikon software, a time lapse was started, capturing images every 5 minutes for a duration of 15 hours. A z-resolution of 1.5 µm was used for experiments not involving soft PDMS, and 0.5 µm otherwise, to allow

more precise tracking of the beads. Data were recorded in three channels: Dendra2, SiR Actin, SPY-595 (Nuclei).

2.3.3 Second and Third Harmonic Imaging

Imaging was performed with the assistance of Dr. Mišo Mitkovski at the City Campus Light Microscopy Facility, Max Planck Institute for Multidisciplinary Sciences. A LaVision TriM Scope II multiphoton microscope was used for all acquisitions. The system was equipped with an XLPLN25XWMP2 water immersion objective (1.05 numerical aperture; Evident Scientific) and a CRONUS-2P laser (Light Conversion) as the excitation source. Second harmonic generation (SHG) and third harmonic generation (THG) signals were detected using non-descanned PMT2 and PMT5 channels, respectively. The transmitted light channel was utilized to optimize the signal-to-noise ratio for each acquisition.

2.4 Cell adhesion measurement

2.4.1 Microfluidic device

To measure the relative substrate adhesion of cells in different conditions, we made a microfluidic chip to apply a shear flow and thus, detach cells.
First PDMS was made by mixing Sylgard 184 Silicon elastomer base and curing agent at a ratio of 10:1. The mixture was degassed using a vacuum desiccator and subsequently poured onto silicon wafer moulds. These moulds featured inverted masters with raised cuboidal chambers (the negative cast of the desired features), the dimensions of which are shown in Figure 2.2. The assembly was then cured in an oven for 90 minutes at 70°C

After this, the base and a plastic petri dish were plasma treated, and subsequently pressed together strongly, and again cured in the oven.
The assembled microfluidic device was connected via PTFE tubing (inner diameter: 0.56 mm, outer diameter: 1.07 mm) to a syringe. Collagen coating was performed according to the protocol in Section 2.2.2 by perfusing the solution through this syringe. Cells were also seeded through the syringe four hours prior to experimentation, after which the device was placed in the microscope incubator for brightfield imaging. The syringe remained

connected to a NEMESYS low-pressure syringe pump system for the duration of the experiment.

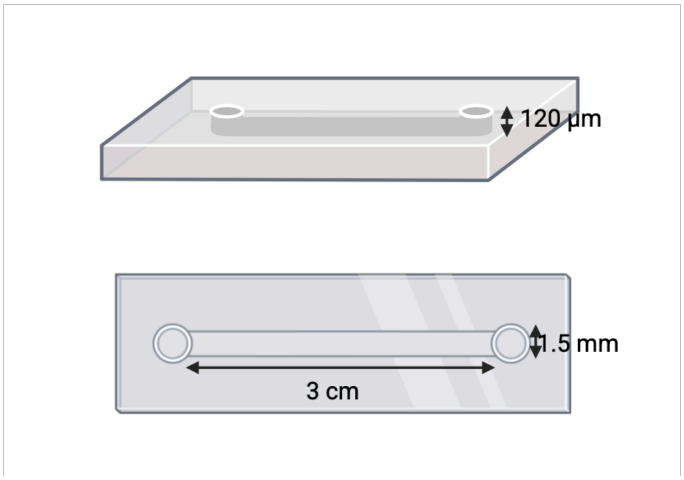

Figure 2.2: Diagram showing the dimensions and shape of the used microfluidic device

2.4.2 Setup of a custom device for centrifugal cell adhesion assay

A second method to measure relative cell adhesion is by detaching cells on a plastic disk in a centrifugal assay due to fluid shear. In order to perform this assay, we developed a custom device for it. Cell culture petridishes (Starstedt) were cut into circular disks of diameter 49mm and was fixed on a magnet using a nut and bolt as shown in figure 2.3.

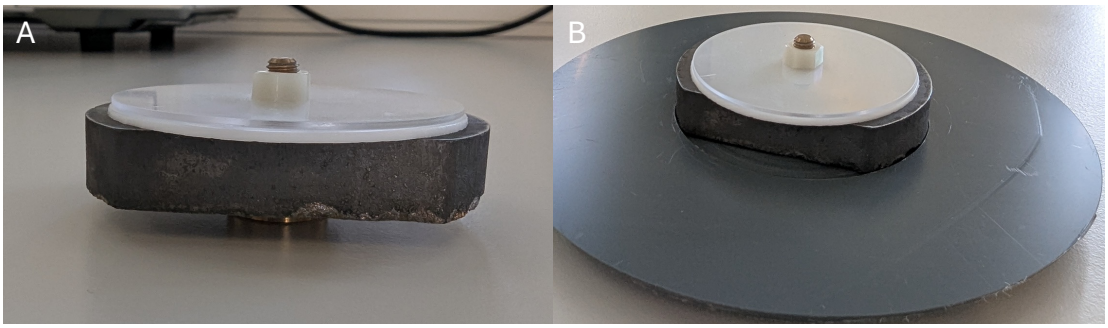

Figure 2.3: Picture showing the circular plastic disk attached to a magnet:*(A) Setup showing how the plastic disk was mounted on the magnet(B) Setup showing how the magnet and the screw head was fit in a custom-made plastic disk with a hollow center.*

The magnet and disk attachment were spun in a beaker using a magnetic stirrer (Lab-Mix 20 by Heidolph).
The screw head is fitted on a custom-made engraved plastic cavity that avoids translatory motion while rotating, thereby also aligns and holds the centres of the magnet and the beaker as shown in Figure 2.3.

The cells were allowed to adhere to the disk for 24 hours in a 10cm Petri dish (Starstedt) with 12ml of media and blebbistatin was added 4 hours before the assay. Cells were treated with 3.3μM Hoechst (Thermo Fisher Scientific) for 30 minutes before washing and imaging, after which it was imaged in brightfield (792 fields of view) and spun while clamped to the magnet for 9 minutes, with an additional 1 minute taken to reach 1000rpm, and 6 seconds to slow down and stop in the end, and the plastic disk was imaged again. For the duration of spinning, the cells were submerged in a spinning buffer containing Dulbecco's PBS solution(AppliChem) with 2mM D-Glucose(Sigma) as mentioned in García et al. (García *et al.*, 1997).

The rotation of the disk draws fluid axially from the surroundings. As the fluid approaches the disk surface, it acquires rotational motion and is forced to exit radially. Under steady laminar flow conditions, the velocity, temperature, and concentration boundary layer thicknesses remain constant for a given rotational speed and are independent of radial distance. This makes the disk a uniformly accessible surface with a uniform diffusive field over its entire surface.

The fluid in direct contact with the disk has the same tangential velocity(u) as the disk surface. The fluid farther away from the disk slows down due to dissipation. This sets up a velocity gradient (∂u/∂z) perpendicular to the disk surface. This gradient produces shear stress at the plastic disk (σ_{ad}), for which formulas to calculate it have been derived – for example, as mentioned in Garcia et al.(García *et al.*, 1997):

$$\sigma_{ad} = 0.800r(\rho\mu\omega^3)^{\frac{1}{2}}$$

where:

- r is the radial distance from the center
- ρ is the fluid density; $1.00 \times 10^3\ kg \cdot m^{-3}$

- μ is the dynamic viscosity; $6.59 \times 10^{-4}\ kg \cdot m^{-1} \cdot s^{-1}$(dynamic viscosity of water at 37°C, approximated for PBS),
- ω is the angular velocity; 104.72 rad/s (angular velocity at 1000 rpm)

The boundary layer thickness (δ) is the zone where velocity is fairly linear. Cells within this layer can be considered to experience a constant shear stress equal to the one at disk surface.

The boundary layer thickness δ can be approximated as:

$$\delta = 3.6\left(\frac{\mu}{\rho\omega}\right)^{\frac{1}{2}}$$

For 1000 rpm, the resulting boundary layer thickness is $\delta = 2.86 \times 10^{-4}$ m. Cells are ~20 μm tall, so they are fully embedded in the high-shear region, and the shear on them can be assumed to be that on the plastic disk.

The presented formulas hold in the infinite disk approximation (disk radius R much larger than δ) and for laminar flow. For the disk used in this study (R = 24.5 mm), the infinite disk approximation is valid, as $R/\delta = 85.66$. For 1000 rpm, the characteristic Reynolds number ($Re = \rho\omega R^2/\mu$) is 3.4×10^4, confirming laminar flow ($Re_{crit} = 3.6 \times 10^5$)(García *et al.*, 1997)

2.5 Calcium Phosphate Transfection

Calcium phosphate transfection protocol was adopted with some optimizations from (Guo *et al.*, 2017). Cells were trypsinized and seeded such that they reached 80% confluency at the time of transfection. For preparation of the DNA-calcium phosphate complex, pcDNA3 H2B-mCherry (Addgene) and pEGFP-N1 H2B-GFP (Addgene) plasmids were used at 2 μg each. DNA was mixed with 15 μL of 2 M $CaCl_2$ and sterile water to a final volume of 140 μL (Solution 1). This solution was added dropwise into 140 μL of 2× HBS buffer (pH 7.05–7.1) while vortexing gently, and the mixture was incubated at room temperature for 15 minutes to allow precipitate formation.

For preparation of the transfection medium, 25 µM chloroquine was added to the culture medium, and 280 µL of the DNA-calcium phosphate precipitate was mixed with 1 mL of the chloroquine-containing medium. The existing medium from the cells was aspirated and replaced with 2 mL of transfection medium (MEM supplemented with 10% FBS, 25 µM chloroquine, and the precipitate) per well. Cells were incubated at 37 °C with 5% CO_2 for 6–16 hours.

Eighteen hours after transfection, the medium was aspirated and replaced with 2 mL of fresh medium. On the second day post-transfection, the medium was replaced with fresh medium containing 0.3 mg/mL G418 to begin selection. Cells were maintained under standard culture conditions, with the G418-containing medium changed every 2–3 days.

2.6 Analysis of data

2.6.1 Analysis of time lapse data

The code for the analysis of cell dynamics and dome kinetics was written in Matlab by Dr. Stefano Villa. Analysis of the acquired data was done by quantifying the movement of cells using Particle Image Velocimetry in the PIVLab tool in Matlab (Thielicke, W., 2014). The mesh size for the PIV analysis was chosen in order to be of the same order of the typical cell size. From the velocity fields obtained from PIVLab, the following parameters were computed:

- Center-of-mass velocity(v_{cm}):

  $$v_{x_{cm}}(t) = < V_x >_{\vec{X}}$$ and similarly for y

  where $< \cdots >_{\vec{X}}$ denotes the spatial average over the field of view in the X direction.

  $$v_{cm} = \sqrt{v_{x_{cm}}^2 + v_{y_{cm}}^2}$$

- root-mean-square (RMS) velocity(v_{rms}):

$$v_{rms}(t) = \sqrt{< [(V_x - v_{x_{cm}})^2 + (V_y - v_{y_{cm}})^2] >_{\vec{X}}}$$

2.6.2 Segmentation of Nuclei Captured via Confocal Microscopy

For nuclei segmentation, Python 3.11.14 with Cellpose was used, with installation conducted via pyenv. Within this version, a virtual environment containing Cellpose 2.0 (cellpose version 4.0.7) was created. Cellpose is a machine learning-based tool that supports human-in-the-loop training and comes pre-trained for segmenting nuclei and cells.

The native Cellpose algorithm was trained using labels derived from multiple z-sections, time frames and different domes across five datasets. Training was performed iteratively: first, non-nuclear detections were removed and segments were manually drawn over any nuclei missed in the initial dataset. The resulting model was then used to refine accuracy on subsequent datasets. This process was repeated sequentially for all datasets.

The final trained model was exported as a .ONNX file for use in Arivis. Within Arivis Pro 4.3.0, images were first denoised using a discrete Gaussian filter with a 1 µm diameter. Segmentation was performed using our custom-trained model. To separate nuclei that were incorrectly merged due to proximity, the segmented objects were split using an optimized split sensitivity parameter of 56%.

All nuclei were then tracked using the software's native tracking feature, selecting the motion type as Brownian, and the tracking data was exported to an Excel file. This output was further analyzed using a MATLAB script written by Dr. Stefano Villa to visualize nuclei. As the nuclear stain produced some non-cellular fluorescent noise above the cells, these points were manually removed from the analysis (less than 2% of the points per time frame).

2.6.3 Cell Counting for the Adhesion Assay

Images were captured continuously using an epifluorescence microscope, with the sample secured on a circular coverslip held within a Petri dish featuring a central circular holder. Following image acquisition, cells were counted using a semi-automated analysis pipeline. Cells were treated with 3.3µM Hoechst (Thermo Fisher Scientific) for 30 minutes before washing and imaging.

The analysis began with a Fiji macro designed to compile images for efficient review. For each experimental condition and timepoint, the macro opened the multi-frame image stacks acquired. It then generated a new, large 16-bit canvas formatted for a 52x10 tile grid. This canvas was populated in a zigzag order. This process interleaved the two stacks into a single montage.

Cell nuclei within the montage were segmented and counted using the TrackMate plugin. A consistent diameter setting of 16.9 µm was applied. The sensitivity threshold was selected by analyzing the software's histogram, which displays a characteristic bimodal distribution, with the first peak corresponding to the noise and the second peak corresponding to the nuclei. To avoid the erroneous segmentation of background noise, a threshold value was chosen immediately after the first peak. This same threshold value was applied to both montages—before and after spinning—to ensure uniform detection. TrackMate recorded the count and the X-Y coordinates of all identified nuclei.

Finally, the ratio of cells remaining after spinning versus those present before as a function of the shear force experienced by the cells (which in turn is a function of the radial distance), was analyzed by Dr. Stefano Villa. This calculation was performed by comparing cell counts within the same radial position before and after the procedure.

2.6.4 Verification of the Rotational Speed of the Custom Cell Adhesion Assay Device

To verify the rotational speed of the magnet on the magnetic stirrer, a Phantom camera VEO4K 990L was used to record the rotating disk at 1400 frames per second. The resulting videos were analyzed in Fiji by measuring 10 time periods, where a time period was defined as the duration required for a marked point on the magnetic disk to return to its original position. The experiment was also made with 1800ml, which is the same quantity of spinning buffer used in experiments.

2.6.5 Analysis including Voronoi tesselation, divergence, dome collapse

Cell area on the substrate and on the dome has been obtained using Voronoi tessellation upon the nuclei centers of mass obtained from Cellpose. The analysis considered the non-planarity of the domes by projecting the Voronoi vertexes on a surface interpolating the nuclei. An average has then been made inside and outside the dome.

Divergence was computed from PIV data using the matlab 'divergence' function. For each experiment, it has been interpolated at the (x,y) coordinates where a new dome was forming at the time points preceding the dome formation. For each condition, this quantity has been averaged over all the domes after shifting the time scale to have t=0 at the dome formation. Only new domes have been considered and not the domes formed after a collapse.

The average dome evolution has been evaluated by averaging the domes areas of all the domes present in a sample after scaling and normalizing them.
The analysis described in this section has all been developed and performed by Dr. Stefano Villa.

3. Results

3.1 MDCKII domes exhibit a characteristic autofluorescence

3.1.1 Autofluorescence intensity correlates with dome growth and collapse

While imaging MDCKII monolayers, we observed an unexpected autofluorescence signal within domes. We therefore characterized this phenomenon to determine its origin and utility for dome tracking.

MDCKII cells exhibit a characteristic autofluorescent lumen. The signal is visible using the FITC channel, with excitation and emission spectra peak at 498 nm and 517 nm respectively. As shown in the time series in Figure 3.1, autofluorescence intensity increases as the dome grows, then decreases and finally vanishes upon collapse. These images were acquired four days post-seeding.

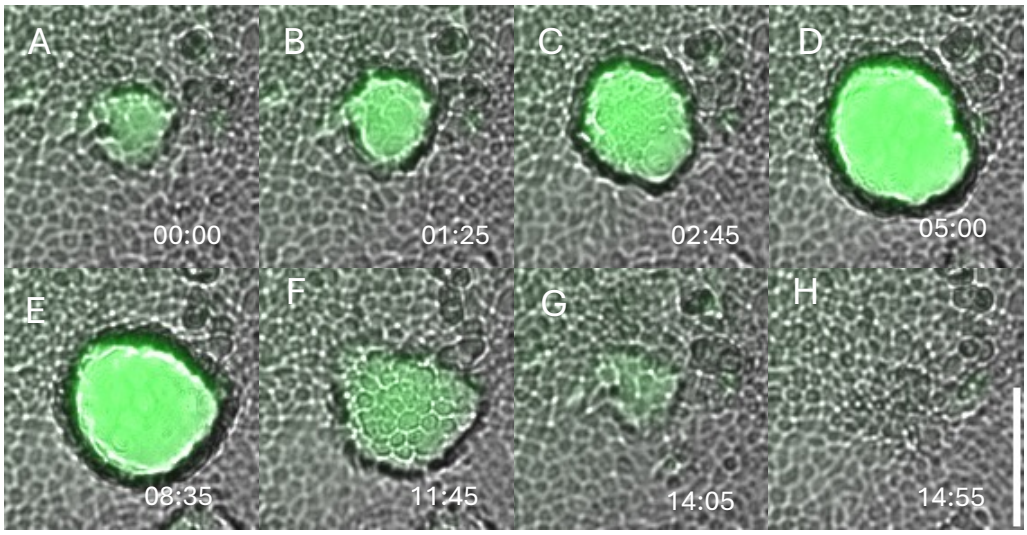

Figure 3.1: Timelapse of dome formation and collapse exhibiting autofluorescence. *Combined brightfield (gray) and epifluorescence (inherent autofluorescence, green) imaging shows a dome forming, growing, and collapsing. Time 0 was 4 days, 9 hours, and 6 minutes post-seeding. Time format is hh:mm. Scale bar in H represents 200 µm.*

3.1.2 Autofluorescent material is transported to the basal side

To determine whether this autofluorescence results from secretions or the pumping activity of MDCKII cells, we grew cells on a permeable polycarbonate membrane. This setup allows monolayer formation while separating the apical and basal compartments, enabling

collection of medium from each side(refer to section 2.2.5). We collected spent medium on day five and day seven post-seeding and measured its autofluorescence intensity. As shown in Figure 3.2, the medium collected from the compartment below the cells showed significantly higher fluorescence intensity compared to the medium above.

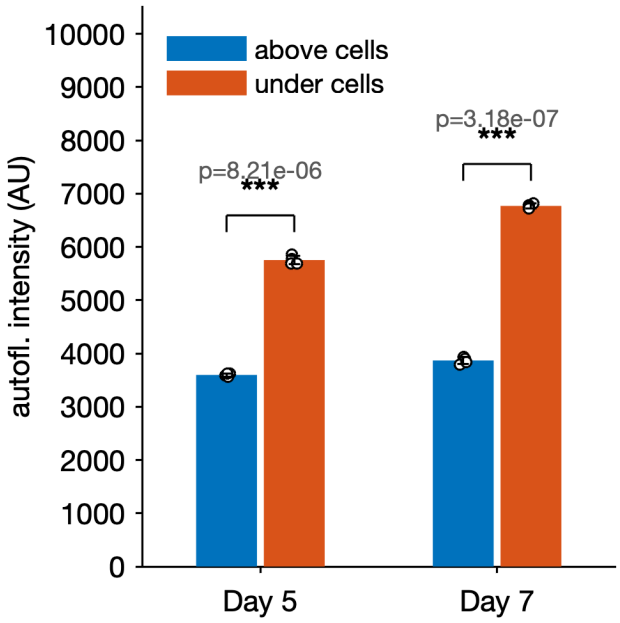

Figure 3.2: Autofluorescence intensity of spent medium from apical and basal compartments. *Bar plots represent mean fluorescence intensity values (arbitrary units) for medium collected from the compartment above the cells (apical) and below the cells (basal) on day five and day seven post-seeding. Fluorescence measurements were performed at Ex/Em of 498 nm and 517 nm. Paired one-tailed t-tests with the hypothesis that medium above cells has lower autofluorescence yielded: Day 5: t(3) = -51.1849, p = 8.21e-06; Day 7: t(3) = -151.4005, p = 3.18e-07.*

3.1.3 Autofluorescence is not specific to a particular MDCKII subline

Since cells cultured over extended periods in the lab may accumulate mutations across generations, we sought to verify whether this autofluorescence is specific to our subline. We therefore ordered MDCKII wild-type cells directly from Sigma. As shown in Figure 3.3, these freshly acquired cells exhibited autofluorescence patterns similar to our lab's existing line. In confocal images, we also observed autofluorescence localized between cells. The precise source and function of this intercellular autofluorescence remain to be

determined.

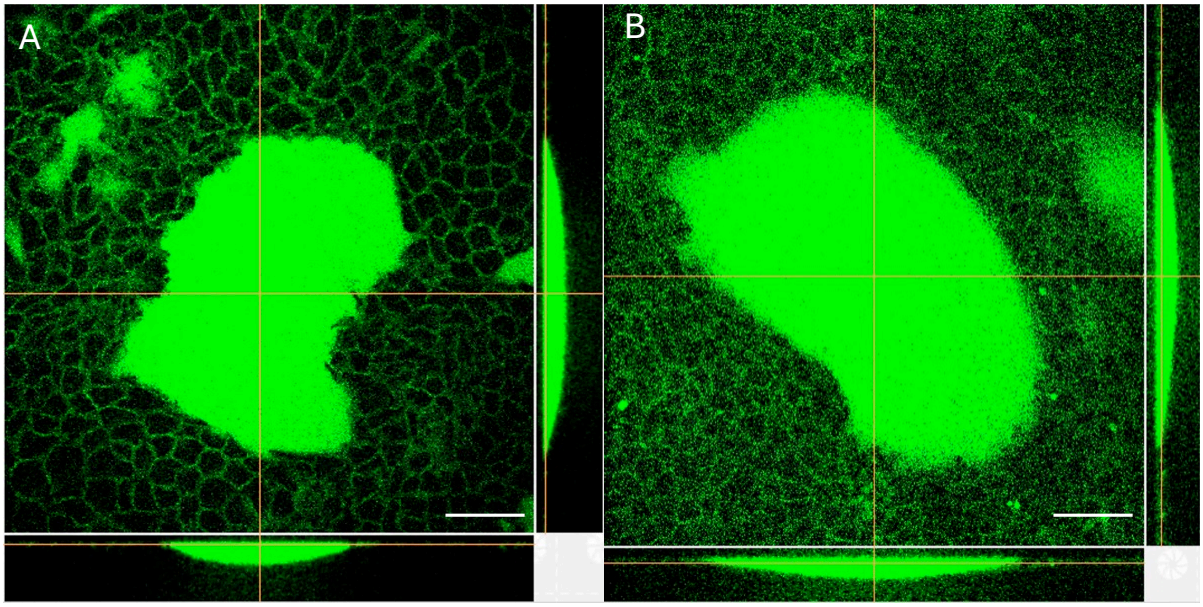

Figure 3.3: Confocal images of autofluorescence in MDCKII domes from different sources. *(A) Confocal image of a dome from MDCKII cells received from Dr. Janshoff's lab. (B) Confocal image of a dome from MDCKII wild-type cells ordered from Sigma. In both (A) and (B), the right panel shows the YZ view, and the bottom panel shows the XZ view, and the yellow lines on the central XY panel indicate the positions used for XZ and YZ projections. Scale bar represents 50 µm (n = 8 dome pairs).*

3.2 Dome structure and morphology

To characterize and to gain a better understanding of our model system we examined dome structure and the potential role of extracellular matrix remodeling.

3.2.1 Domes exhibit variable shapes and sizes on uniform collagen coatings

As visualized by fluorescence microscopy, domes grown on a uniform layer of 4 µg/mL collagen—the standard condition for all experiments unless stated otherwise—exhibit highly irregular shapes. Some domes display jagged edges or indentations, while others appear more circular. Dome sizes also show high variability, as shown in Figure 3.4.

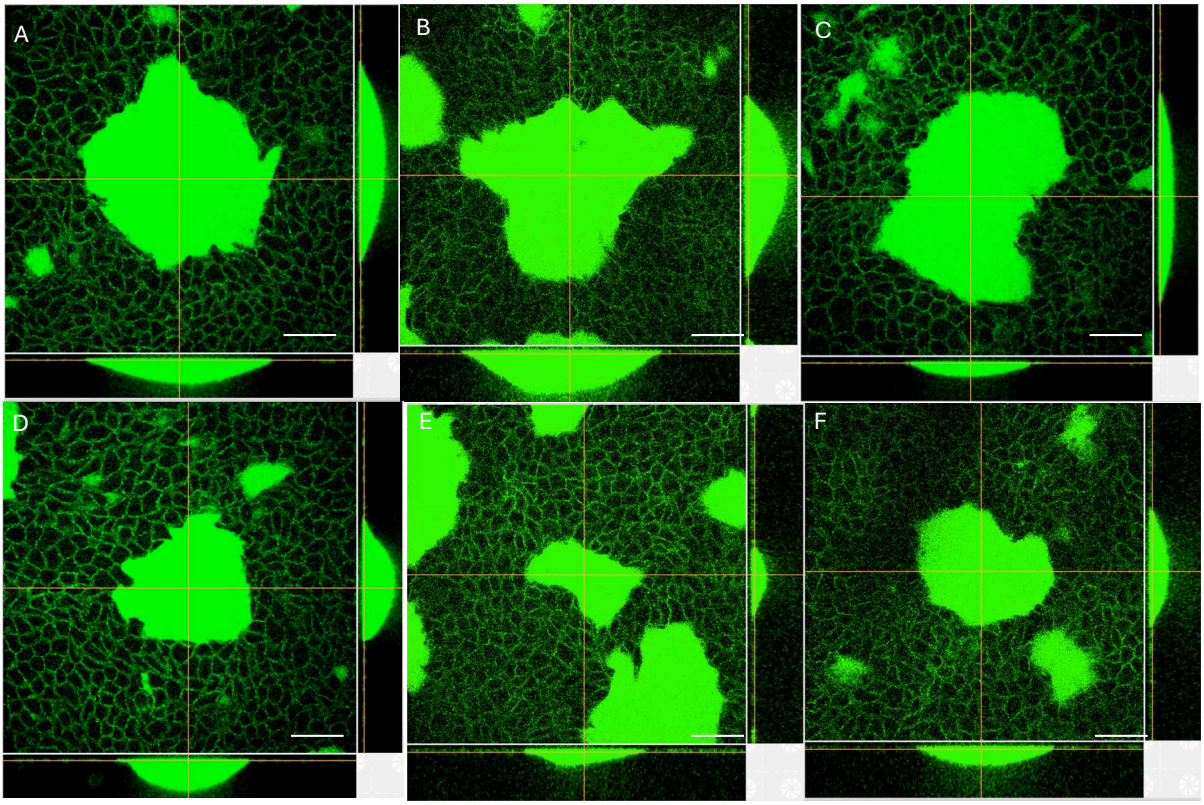

Figure 3.4: Structure and shape of MDCKII domes*. Images A-F show XY, XZ, and YZ sections of domes visualized through the autofluorescence channel. Each dome exhibits a unique shape and size. Images were acquired approximately 90 hours post-seeding. Scale bar represents 50 µm.*

3.2.2 Second harmonic generation reveals no collagen remodeling within domes

To investigate whether the collagen used for coating is remodeled within the dome, we employed label-free imaging using second harmonic generation (SHG). This technique uses two incident photons on a non-centrosymmetric object (such as collagen fibres or microtubules) to produce a single photon at twice the frequency (van Huizen *et al.*, 2019). As shown in Figure 3.6, no difference was observed between domes grown on collagen-coated substrates and those grown without collagen when imaged with SHG. This suggests that if collagen is present within the dome, it is not in an organized, fibrillar form detectable by SHG, indicating that extensive remodeling into crosslinked fibers is not a feature of dome formation in our system.

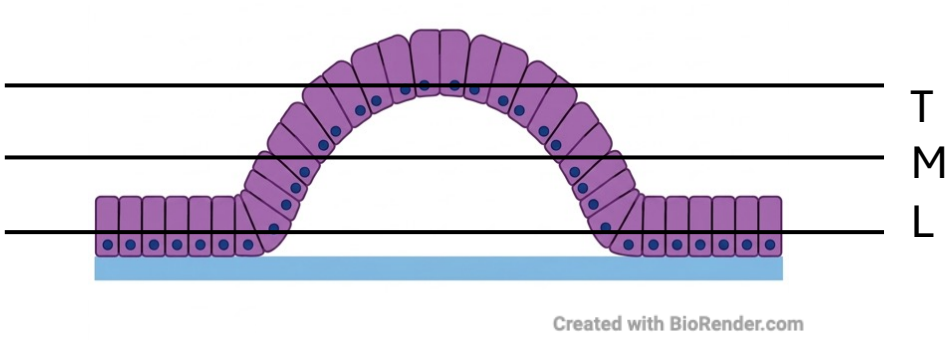

***Figure 3.5: Cross-section of domes shown in subsequent images**. Cross-sections taken at the top layer, middle layer, and lowermost layer are shown as a visual representation of the focal planes at which images in Figures 3.6 and 3.7 were captured.*

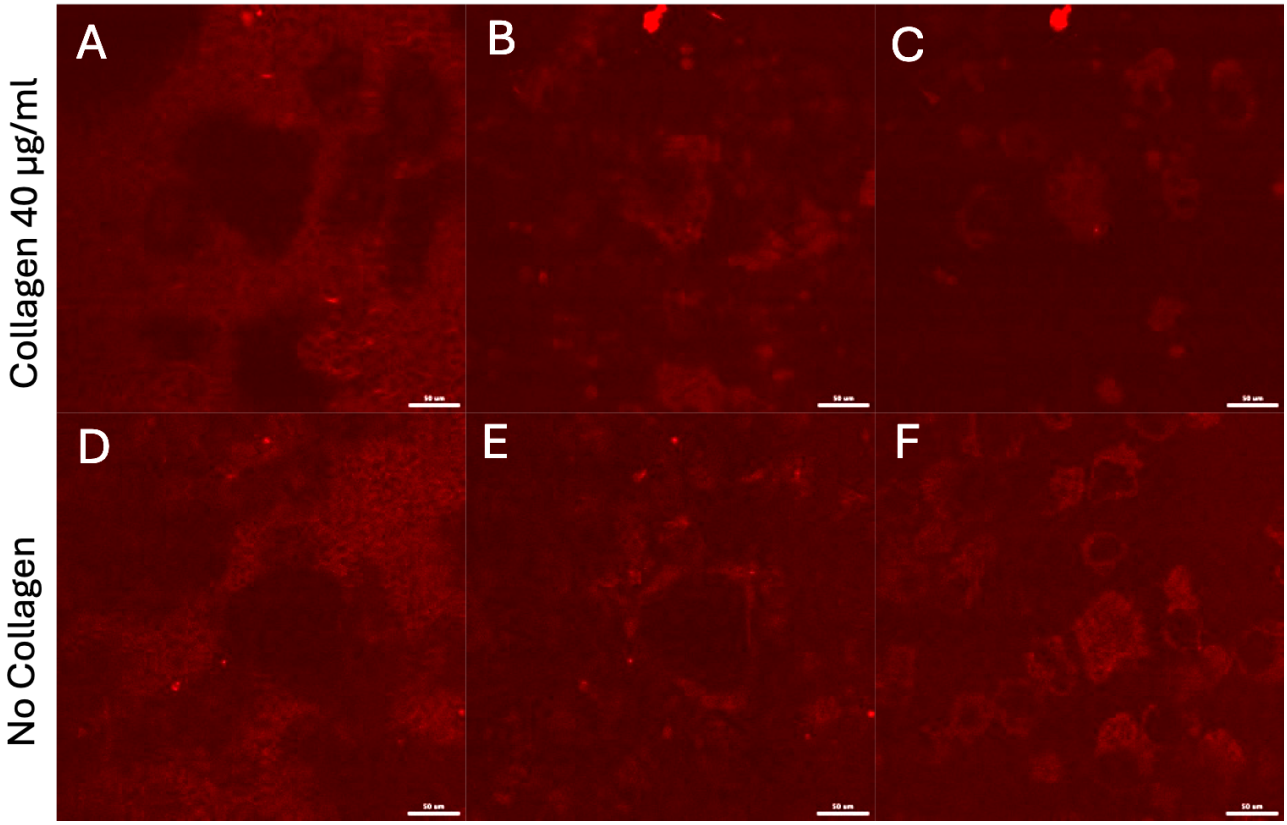

***Figure 3.6: Second harmonic generation (SHG) images of domes**. Images A-C and D-F represent the lower, middle, and top layers (refer to Figure 3.5) of a dome grown on a uniform layer of treated 40 µg/mL collagen and on no collagen, respectively.*

3.2.3 Third harmonic generation detects an uncharacterized substance beneath domes

We also performed third harmonic generation (THG), which operates on a similar principle but uses three incident photons to generate a single photon at three times the frequency. As shown in Figure 3.7, we observed a very strong signal at the base of the dome, present specifically in the area beneath the dome but not in regions where cells remained adherent to the surface. THG is known to indicate boundaries where refractive index changes occur, such as lipid-water and to a lesser extent protein fiber-water interfaces (van Huizen *et al.*, 2019). This unknown substance observed beneath domes remains to be characterized.

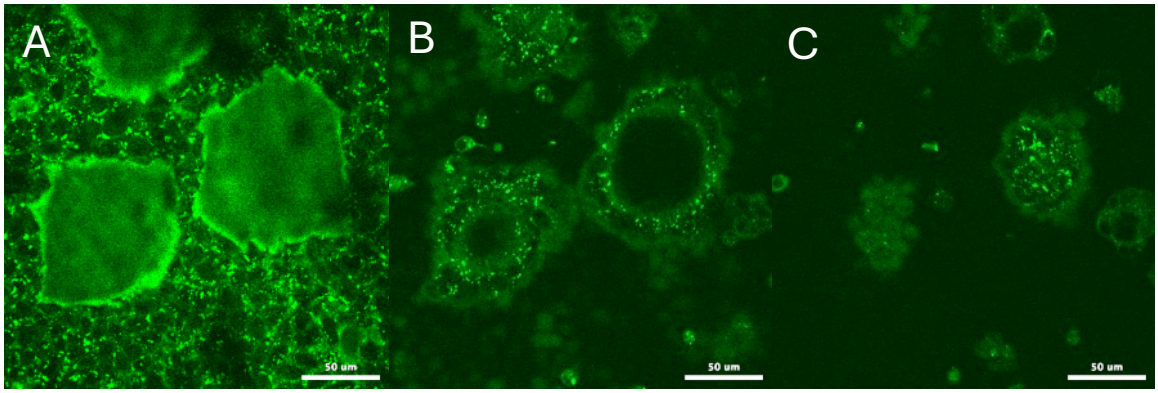

Figure 3.7: Third harmonic generation (THG) images of a dome. *Images A-C represent the lower, middle, and top layers of a dome (refer to Figure 3.5) as visualized by THG.*

3.3 HGF and Blebbistatin modulate MDCKII collective dynamics and dome formation

3.3.1 HGF increases cell motility in a dose-dependent manner

In order to tune cellular velocity, we selected Hepatocyte Growth Factor (HGF) to increase it and blebbistatin to decrease it. Both have strong, tested effects. HGF increases cell motility in human trophoblasts by influencing MAPK and PI3-kinase pathways (Cartwright *et al.*, 2002). Hyperactive HGF signaling is also implicated in cancer survival and growth (Fu *et al.*, 2021). Blebbistatin is a small molecule inhibitor of Myosin II (Kovács *et al.*, 2004).

To observe how cell dynamics change upon HGF addition, we first followed cells under various concentrations of HGF. As seen in Supplementary Figure 5.3, there is a direct correlation between v_{rms} and increasing HGF concentration. The center-of-mass velocity v_{cm} represents the average velocity of a system and is indicative of collective cell motion. The root-mean-square (RMS) velocity v_{rms} measures the magnitude of velocity fluctuations after removing the average motion and represents internal cellular agitation (see Section 2.6.1 for formulas). This correlation indicates that HGF successfully increases cell motility. Large changes were observed at HGF concentrations of 40 and 80 ng/mL, so these two conditions were selected for longer experiments. All conditions showed a sharp increase in velocity.

All imaging and drug additions were initiated 2 days post-seeding, as this is when cells reach confluency. As seen in Figure 3.8, the peak in cell velocity following the stress of experimental setup—attributed to the concurrent recovery and mitotic activity during this transitional period—was most pronounced in HGF-treated samples. HGF-treated samples exhibited higher peak velocities for both v_{cm} and v_{rms}, indicating that HGF stimulates more dynamic collective cell movements and internal agitation compared to the control during this window of heightened motility.

The HGF 80 ng/mL condition reached the highest peak velocity, followed by HGF 40 ng/mL, and then the control, demonstrating a dose-dependent effect of HGF on increasing velocity during the recovery period. After reaching peak velocity, all conditions gradually decreased.

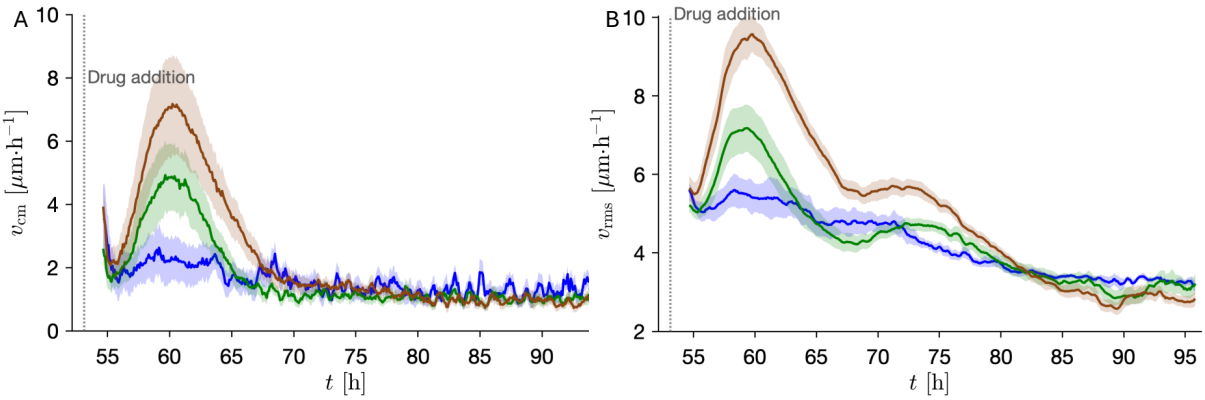

Figure 3.8: Collective dynamics of MDCKII cells under different concentrations of HGF. *The figure shows how v_{cm} and v_{rms} change over time when HGF at concentrations of 0 (blue), 40 (green), and 80 (brown) ng/mL were added. T=0 represents the time of cell seeding, (n=3). T=0 represents the time of cell seeding. Solid lines represents the mean; shaded area denotes ±1 SD. (Code written by Dr. Stefano Villa).*

3.3.2 Blebbistatin and PDMS substrate modulate cell motility and dome morphology

Blebbistatin was our candidate for reducing motility, as it inhibits Myosin II. As shown in Figure 3.5B, blebbistatin treatment decreased v_{rms} for approximately 12 hours post-treatment, confirming successful suppression of cell motility.

For PDMS substrates, we sought to further investigate the preliminary observations shown in Figure 1.1, where cells grown on PDMS exhibited altered dome dynamics compared to plastic. Cells grown on PDMS showed an initial increase in v_{cm} and consistently higher v_{rms} than the control throughout the time course (Figure 3.10A, B), consistent with our earlier findings that reduced adhesion correlates with increased cell agitation.

Due to time constraints, we selected the blebbistatin and PDMS conditions for further experiments, as they exhibited considerably different dome morphologies (Figure 3.9) and we were interested in decoding the mechanisms underlying these differences. For these selected conditions, cells were imaged in both brightfield and autofluorescence channels to quantify dome size, number, growth, and collapse over time. The

autofluorescence of domes enabled segmentation and tracking of dome evolution for detailed analysis of number, size, and temporal dynamics.

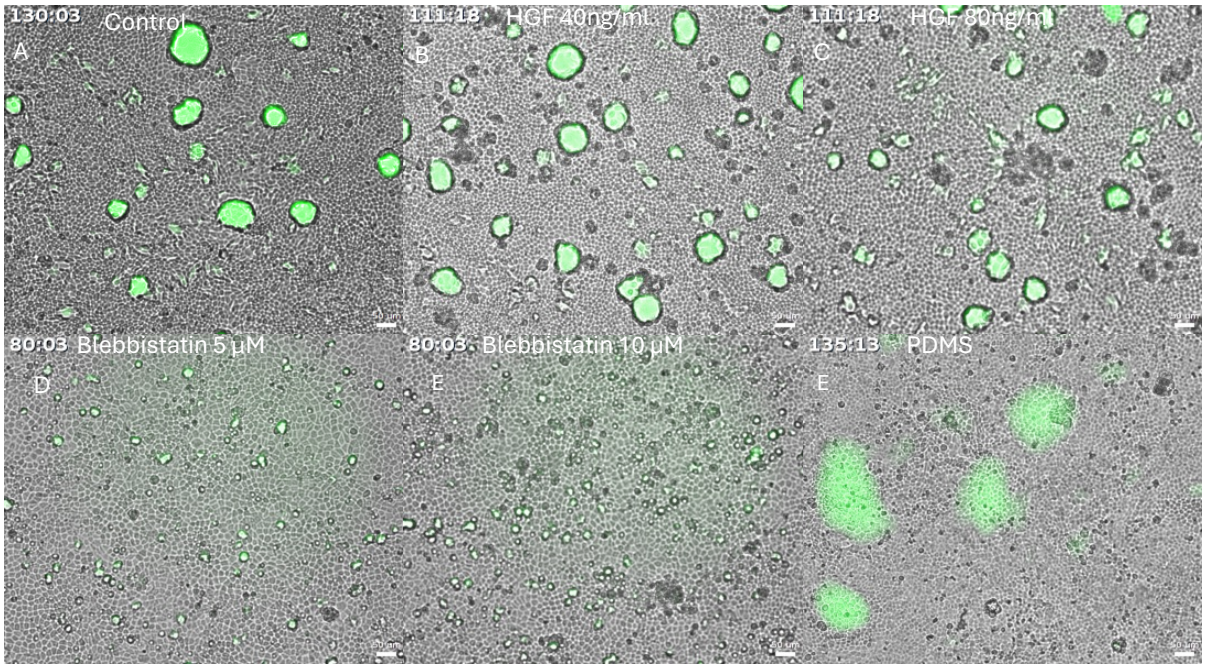

Figure 3.9: Size and structure of domes varies under different conditions*. The images show a superimposition of epifluorescence (inherent autofluorescence, green) marking domes and brightfield imaging (gray). (A) Control. (B) and (C) HGF at 40 and 80 ng/mL, respectively; domes are similar in number and size to control. (D) and (E) Blebbistatin at 5 and 10 µM, respectively; domes are much smaller and more numerous compared to control. Time is represented as hh:mm post-seeding. Fields were chosen to representatively show dome size and number within the field of view.*

3.3.3 Quantitative analysis reveals distinct dome kinetics across conditions

The observed peak in cell velocity following experimental setup can be attributed to a combination of factors. Immediately after the start of imaging, cells experience stress from the change in temperature and environment, which temporarily disrupts their steady state. During this same window, cells also continue to divide as confluency is still not fully reached everywhere in the sample. It is this concurrent stress and mitotic activity—rather than a strictly sequential process—that likely contributes to the heightened motility observed during this transitional period. It is during this time that

the control condition shows a higher velocity of cells, and the effects of blebbistatin and HGF treatments are most clearly distinguishable.

As seen in Figure 3.10A, cells grown on PDMS exhibited a sharp, high peak in v_{cm}, higher than all other conditions from approximately 55–67 hours post-seeding, after which all velocities stabilized at similar levels. The control also showed a moderate increase in velocity during this same period of heightened biological activity, but this increase was absent in blebbistatin-treated conditions (5 and 10 μM). This suggests that the motility reawakening following experimental stress—and the associated peak in cell movement—is inhibited by blebbistatin.

Figure 3.10B shows v_{rms} over time. PDMS exhibited a very sharp, high peak, much higher than all other conditions, indicating significant fluctuations in movement during this transitional period. It remained consistently elevated afterwards. Blebbistatin at 5 μM and 10 μM showed a dose-dependent decrease in v_{rms} for up to 15–20 hours post-treatment. Thus, blebbistatin suppresses both mean and RMS velocities, with higher concentrations (10 μM) showing greater suppression of the motility peak observed during the recovery phase. Across repeated experiments (data not shown), we observed that the timing of this motility recovery varied between samples, but the relative suppression by blebbistatin was consistent.

Figure 3.10D shows mean dome area over time. PDMS displayed a sharp increase in mean dome area, plateauing at the highest values among all conditions. The control showed a gradual increase but remained lower than PDMS. Both blebbistatin conditions showed smaller mean areas and lower plateau values compared to PDMS and control, indicating smaller dome sizes.

Figure 3.10E shows the number of domes over time. Blebbistatin-treated conditions (5 and 10 μM) exhibited a sharp peak in dome number around 80–100 hours, followed by a decline, indicating rapid formation and subsequent collapse of many domes. The control showed a gradual increase in dome number, peaking later than blebbistatin conditions and then stabilizing. PDMS displayed a moderate increase in dome number, peaking and stabilizing at a level lower than the control. From replicate experiments

(data not shown), we noted that the exact timing of the peak in dome number for blebbistatin conditions was sample-dependent, but it consistently coincided with the period when v_{rms} recovered.

Figure 3.10F shows the ratio of detached area to total area over time. PDMS showed a rapid increase in detachment ratio starting around 70 hours, reaching the highest values with some fluctuations indicating ongoing detachment events. The control showed a gradual increase starting around 80 hours, eventually reaching values similar to PDMS from approximately 125 hours onwards, suggesting a steady accumulation of detachment events. Blebbistatin conditions showed a slight increase in detachment ratio peaking around 80 hours, ultimately reaching low detachment ratios, with 10 μM showing a lower plateau than 5 μM. Importantly, while the time needed to reach the plateau varied considerably between experiments—ranging from day 4 to day 6—the final plateau value of the detachment ratio was highly conserved: control and PDMS consistently reached approximately 0.1, whereas blebbistatin conditions stabilized at significantly lower values (data not shown).

Figure 3.10C shows dome half-life over time. Blebbistatin-treated conditions exhibited low and relatively stable half-life values, indicating dynamic changes in dome stability with frequent formation and collapse.

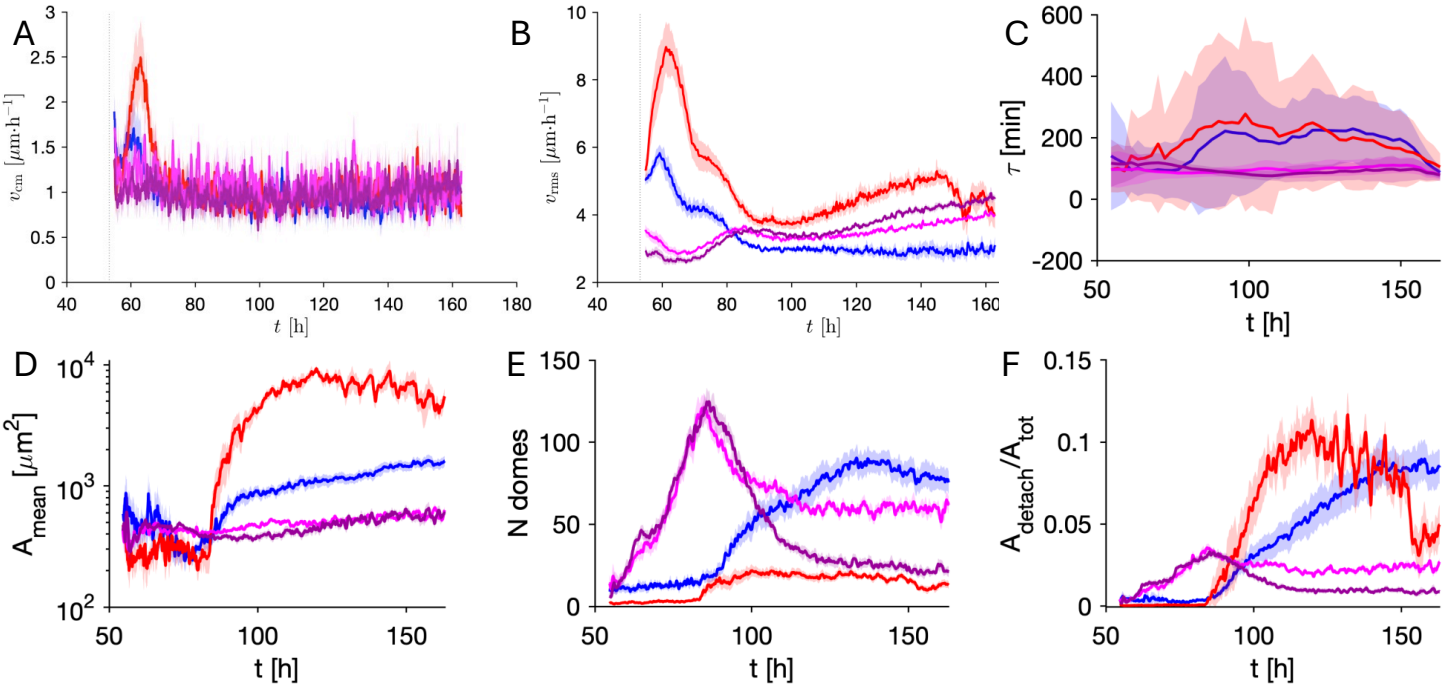

Figure 3.10: Long-term cell dynamics on PDMS and under blebbistatin treatment. *Collective cell dynamics were observed for control, PDMS, and 5 µM and 10 µM blebbistatin. (A) v_{cm} over time. (B) v_{rms} over time. (C) Dome half-life over time. (D) Mean dome area over time. (E) Number of domes over time. (F) Ratio of detached area to total area over time. Red represents PDMS, blue represents control, pink represents blebbistatin 5 µM, and magenta represents blebbistatin 10 µM. T=0 represents the time of cell seeding. Solid lines represents the mean; shaded area denotes ±1 SD. (n=3). (Analysis performed by Dr. Stefano Villa).*

3.4 High-resolution imaging reveals actin dynamics during dome collapse

3.4.1 Actin organization differs between dome cells and surrounding monolayer and dome collapse involves pulling by contractile surrounding cells

To understand the cellular mechanisms underlying the dynamics during dome evolution and collapse, we used high-resolution spinning disk confocal microscopy to visualize the actin and nuclei. We labeled nuclei with SPY595 DNA and F-actin with SiR Actin to track their dynamics. SiR Actin was used along with 5mM Verapamil, which is needed for long term

acquisition. SiR Actin is highly effective for imaging temporally resolved, highly dynamic F-actin populations in live cells (Nasufovic *et al.*, 2025).We separately verified that staining with SiR Actin and verapamil does not affect cell dynamics, as shown in Supplementary Figure 5.1. The actin labeled in this manner consists of two main populations: actin stress fibers, which are present primarily at the base of cells and provide traction and contractility, and the actin cortex, which is present at cell borders at higher planes and provides structural integrity. For data representation, we generate maximum intensity projections of Z-stacks corresponding to stress fibers (labeled in magenta) and the actin cortex (labeled in green), as illustrated schematically in Figure 3.11.

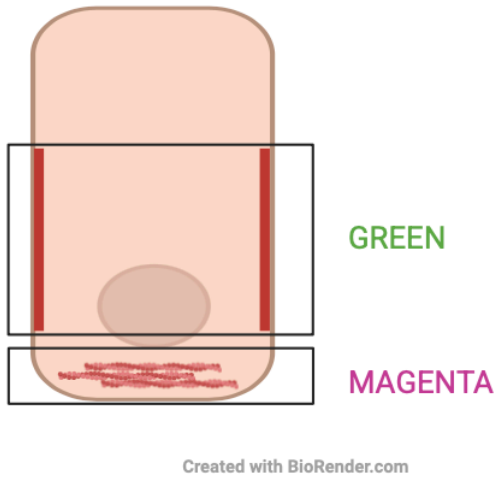

Figure 3.11: Schematic showing the representation of actin fibers and cortex convention used*. Z-stacks comprising actin stress fibers are subjected to maximum intensity projection and labeled in magenta; Z-stacks comprising actin cortex are similarly projected and labeled in green.*

By following actin dynamics during and after dome collapse, we observed significant restructuring of actin and changes in collective cell behavior. We visualized this process using confocal timelapse microscopy with 5-minute intervals, as shown in Figure 3.12. An intact dome, with surrounding cells exhibiting organized actin stress fibers, was visible (Figure 3.12A). The dome 5 minutes before collapse is shown in Figure 3.12B, and the dome immediately after collapse (one frame later) is shown in Figure 3.12C. Using nuclei positions as a proxy, we observed that cells which formed part of the dome moved apart and away from the center 10 minutes after collapse, as if pulled by surrounding cells (Figure 3.12D). Simultaneously, cells from the top of the dome showed no actin stress fibers, only an actin cortex. This suggests that dome-forming cells, lacking stress fibers, are less contractile and are

being pulled outward by the more contractile surrounding cells. By 1 hour and 10 minutes after collapse, actin stress fibers began to reform on cells that were part of the dome, and cells moved back toward the center, pulling themselves back in (Figure 3.12F). As time progressed further, actin stress fibers became homogeneously distributed throughout the field of view (Figure 3.12 G-I). It is known that actin stress fibers help attach cells to the substrate through focal adhesions and provide traction (Kovaleva *et al.*, 2025). This indicates that actomyosin filaments play an active role in both dome maintenance and collapse.

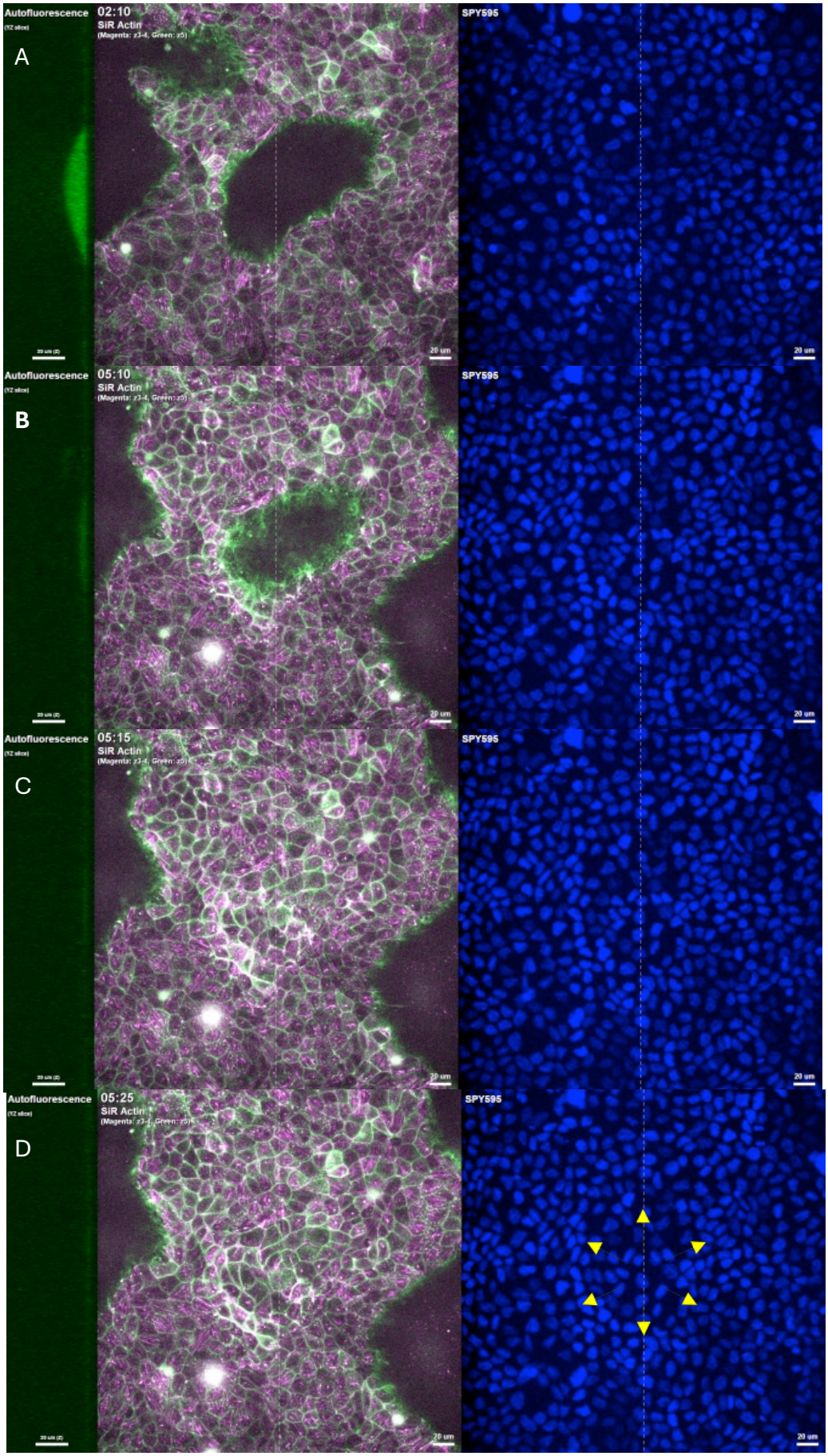
Autofluorescence
(YZ slice)
02:10
SiR Actin
(Magenta: z3-4, Green: z5)
SPY595
A
20 um
Autofluorescence
(YZ slice)
05:10
SiR Actin
(Magenta: z3-4, Green: z5)
SPY595
B
20 um
Autofluorescence
(YZ slice)
05:15
SiR Actin
(Magenta: z3-4, Green: z5)
SPY595
C
20 um
Autofluorescence
(YZ slice)
05:25
SiR Actin
(Magenta: z3-4, Green: z5)
SPY595
D
20 um

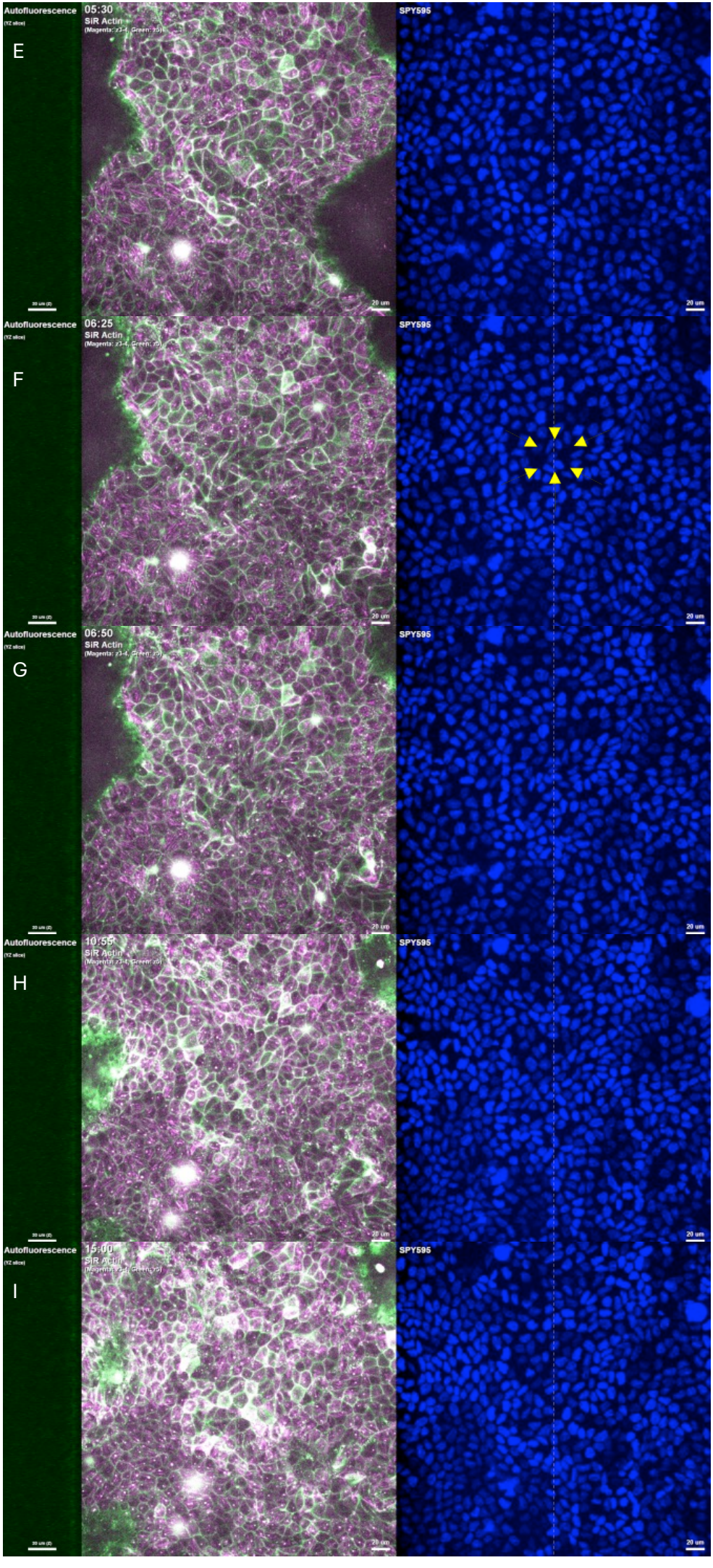
Autofluorescence
(YZ slice)
E
05:30
SiR Actin
(Magenta: z3-4, Green: z9)
20 um
SPY595
20 um
Autofluorescence
(YZ slice)
F
06:25
SiR Actin
(Magenta: z3-4, Green: z9)
20 um
SPY595
20 um
Autofluorescence
(YZ slice)
G
06:50
SiR Actin
(Magenta: z3-4, Green: z9)
20 um
SPY595
20 um
Autofluorescence
(YZ slice)
H
10:55
SiR Actin
(Magenta: z3-4, Green: z9)
20 um
SPY595
20 um
Autofluorescence
(YZ slice)
I
15:00
SiR Actin
(Magenta: z3-4, Green: z9)
20 um
SPY595
20 um

Figure 3.12: Timelapse microscopy images showing dome collapse. *Images A-I show a temporal sequence, each with three panels. Left panel: YZ view of autofluorescence channel marking the dome. Central panel: SiR Actin channel labeled with magenta and green as described in Figure 3.11. Right panel: Maximum intensity projection of all Z-stacks from SPY595 DNA channel staining nuclei shown in blue. Dotted lines in actin and nuclei channels indicate the position from which the YZ projection for the autofluorescence channel was taken. The direction of movement of the nuclei afre indicated with yellow arrows.*

To substantiate our observations quantitatively, we segmented and tracked nuclei over time. Using nuclear positions, we performed Voronoi tessellation to estimate cell areas based on the geometric center of each nucleus. As shown in Figure 3.13A, the area of cells inside the dome increases after dome's collapse, quickly reaching a peak and then gradually decreasing as actin repolarizes into stress fibers and pulls these cells back inward. The v_{rms} for cells inside the dome also spikes during this period, indicating faster movement and higher agitation immediately after collapse, further supporting our observation (Figure 3.13B).

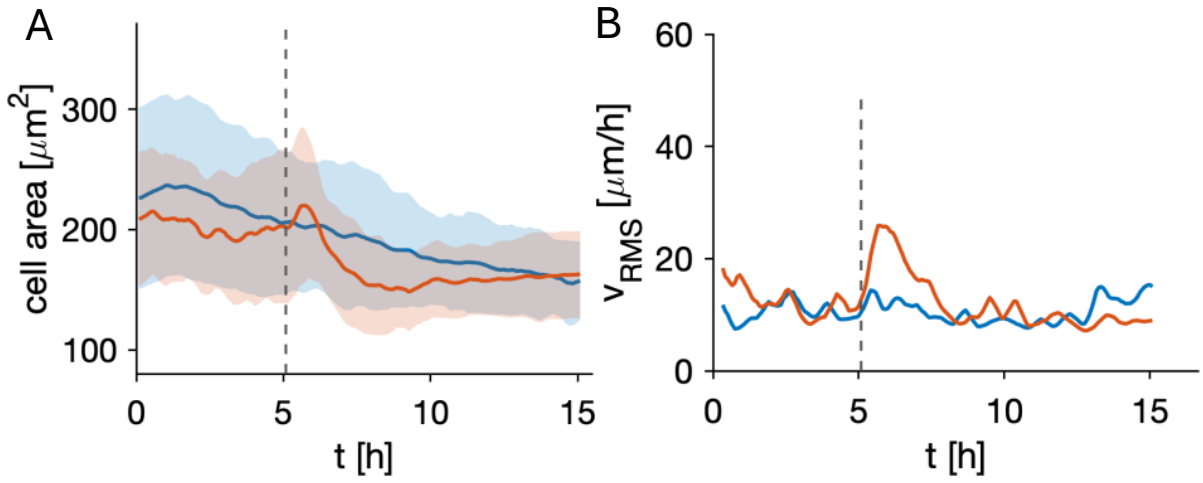

Figure 3.13: Dome kinetics during and post-collapse. *(A) Cell area plotted against time. (B) Velocity RMS (v_{rms}) plotted against time. Cell populations are divided into those outside the dome (pale blue) and those inside the dome (orange). The dotted line represents the time of collapse of the dome. Solid lines represents the mean; shaded area denotes ±1 SD. (Analysis performed by Dr. Stefano Villa).*

3.4.2 Blebbistatin treatment abolishes pulling by surrounding cells and actomyosin-driven recovery after collapse

To test whether this relaxation and contraction is driven by actomyosin contractility, we added 10 μM blebbistatin before imaging domes. As shown in Figure 3.14A, the domes initially appear similar to the control dome in Figure 3.12A, with surrounding cells exhibiting actin stress fibers. Figure 3.14A shows an intact dome approximately 1 hour after blebbistatin addition. Collapse begins approximately 7.5 hours after acquisition (Figure 3.14B). Following collapse, the cells that were part of the dome show no actin stress fibers (Figure 3.14C). Tracking further through time reveals no apparent nuclear movement (Figures 3.10D-F).

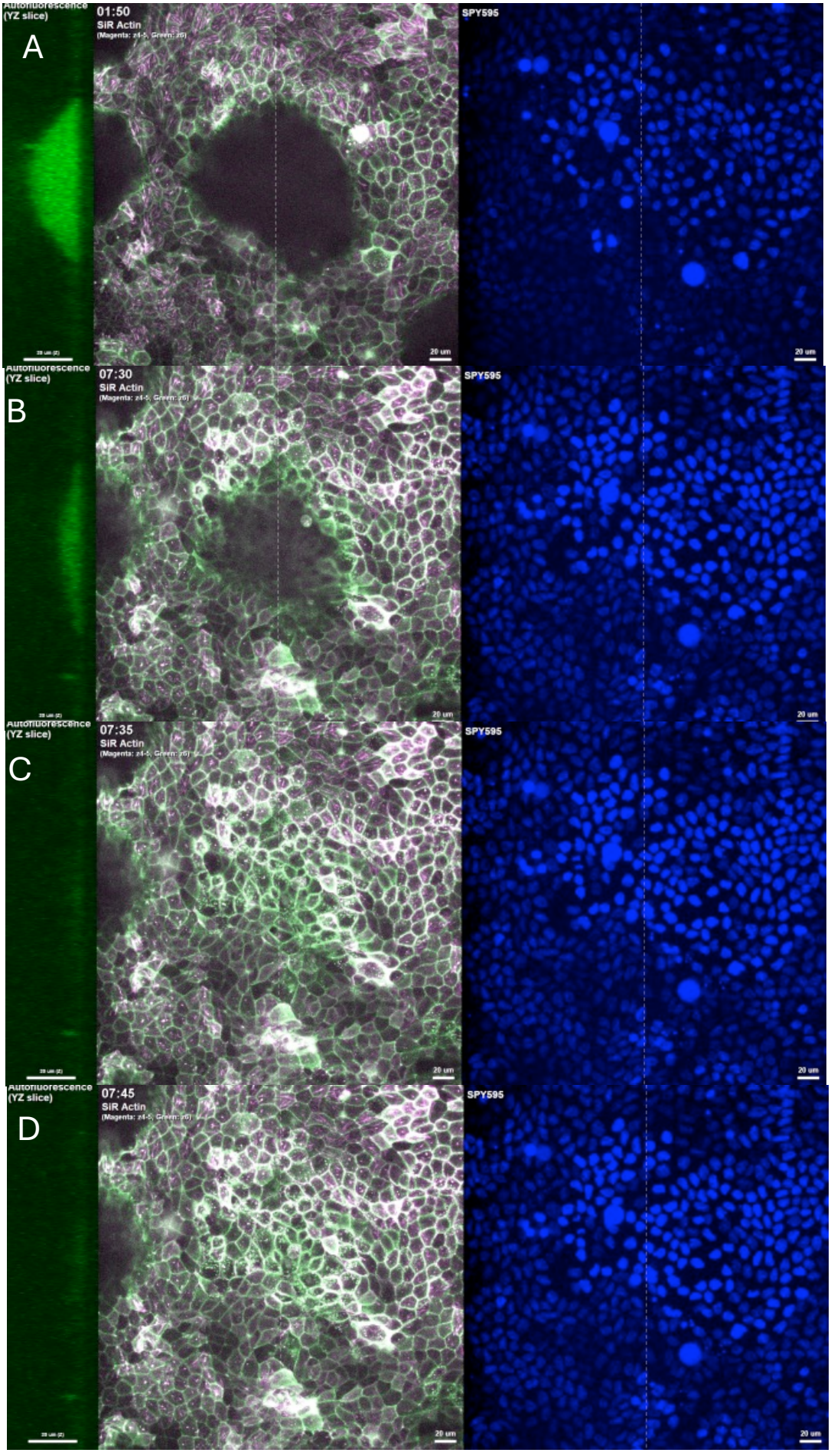
Autofluorescence
(YZ slice)
A
01:50
SiR Actin
(Magenta: z4-5, Green: z0)
SPY595
20 um
B
07:30
C
07:35
D
07:45

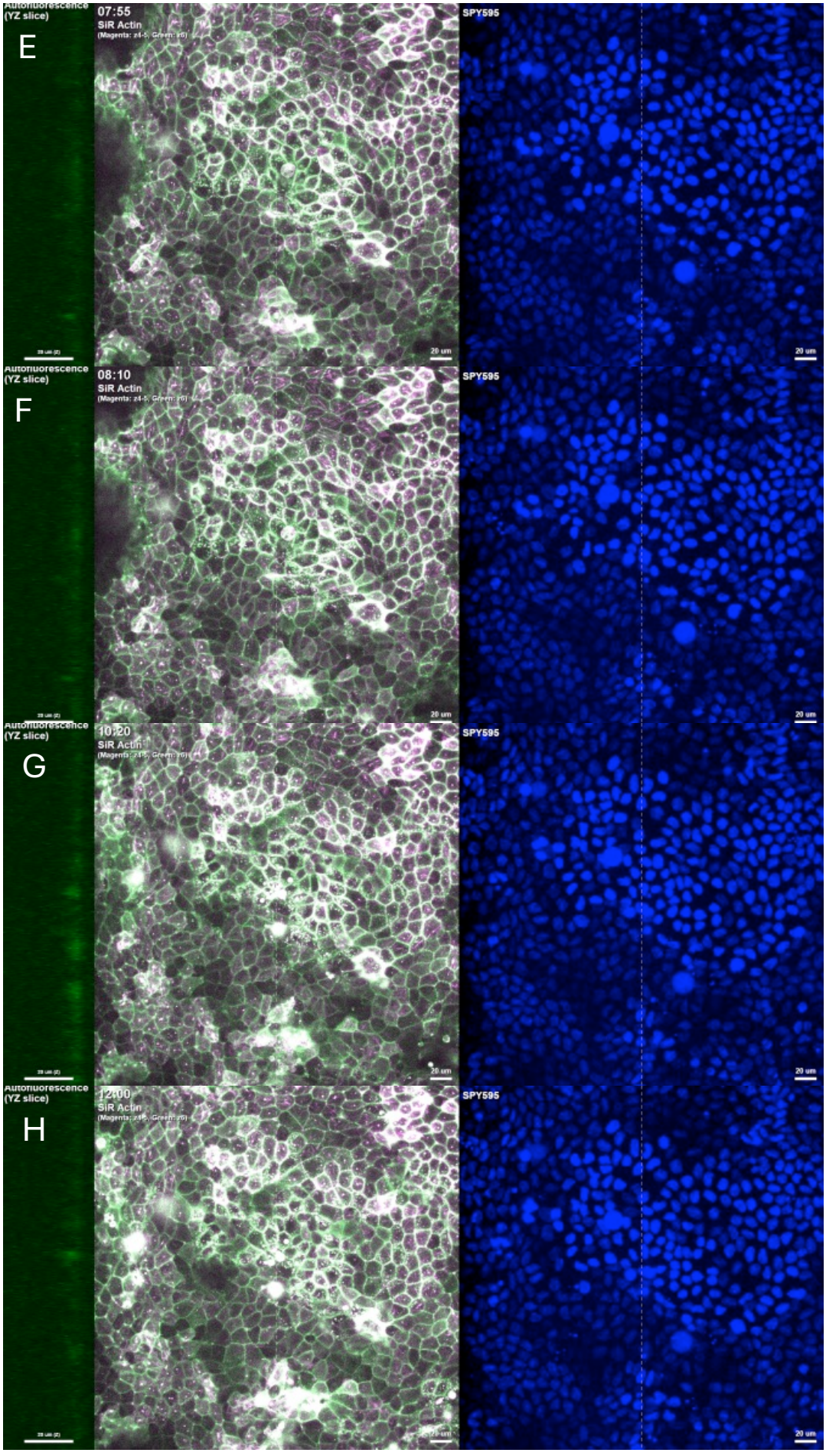
Autofluorescence
(YZ slice)
E
07:55
SiR Actin
SPY595
20 um
F
08:10
G
10:20
H
12:00

Figure 3.14: Timelapse microscopy images showing dome collapse under 10 µM blebbistatin treatment. *Images were acquired starting 1 hour and 14 minutes after blebbistatin addition. Images A-H show a temporal sequence, each with three panels. Left panel: YZ view of autofluorescence channel marking the dome. Central panel: SiR Actin channel labeled with magenta and green as described in Figure 3.11. Right panel: Maximum intensity projection of all Z-stacks from SPY595 DNA channel staining nuclei. The nuclear staining intensity varies because SPY595 does not guarantee equal staining across all cells. Dotted lines in actin and nuclei channels indicate the position from which the YZ projection for the autofluorescence channel was taken.*

As shown in Figure 3.15, there is no change in cell area before and after collapse for cells either inside or outside the dome (Figure 3.15A). The v_{rms} shows only periodic fluctuations (Figure 3.15B). These results confirm that the relaxation and contraction of cells that were part of the dome after collapse is due to the contractile nature of actomyosin filaments in the cells surrounding the dome as opposed to the non contractile nature of the cells that were a part of the dome.

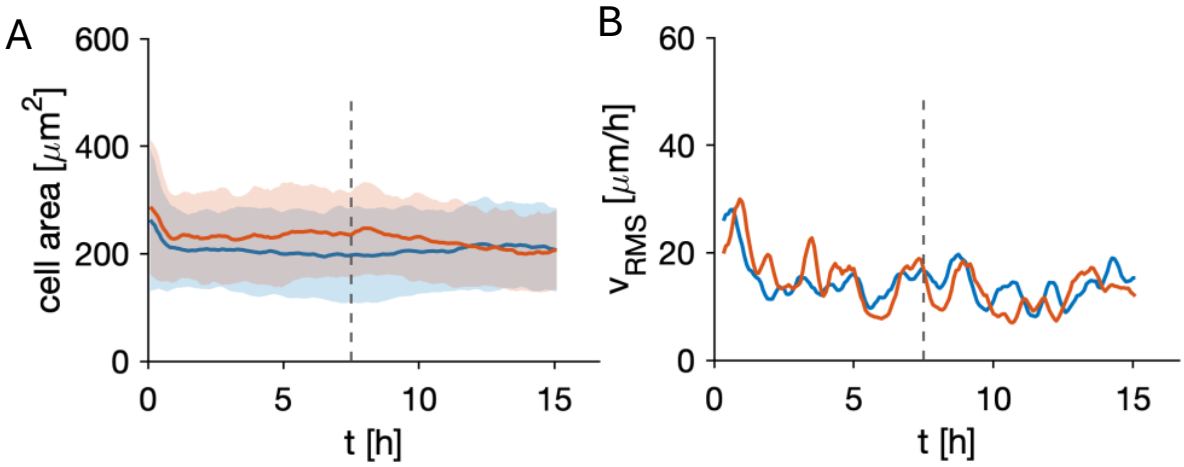

Figure 3.15: Dome kinetics during and post-collapse under 10 µM blebbistatin treatment. *Imaging started 1 hour and 14 minutes after blebbistatin addition. (A) Cell area plotted against time. (B) Velocity RMS (v_{rms}) plotted against time. Cell populations are divided into those outside the dome (pale blue) and those inside the dome (orange). The dotted line represents the time of collapse of the dome. Solid lines represents the mean; shaded area denotes ±1 SD. (Analysis performed by Dr. Stefano Villa).*

This confirms that the post-collapse recovery observed in control cells is actomyosin-dependent, as inhibiting Myosin II with blebbistatin completely abolishes the pulling.

3.5 Dome formation and collapse kinetics are modulated by substrate and treatment

3.5.1 Dome formation correlates with cell dynamics

To complement our population-level analysis of dome numbers and areas, we examined the formation dynamics of individual domes across conditions. We analyzed the divergence of velocity fields from cells that would eventually form a dome. As shown in Figure 3.16, these cells exhibit a decrease in divergence well below zero starting about 20-40 minutes before dome, indicating a consistent inward-directed motion before the detachment. This peak is lower for PDMS-grown cells compared to control, and the peak for blebbistatin-treated conditions cells is lower still.

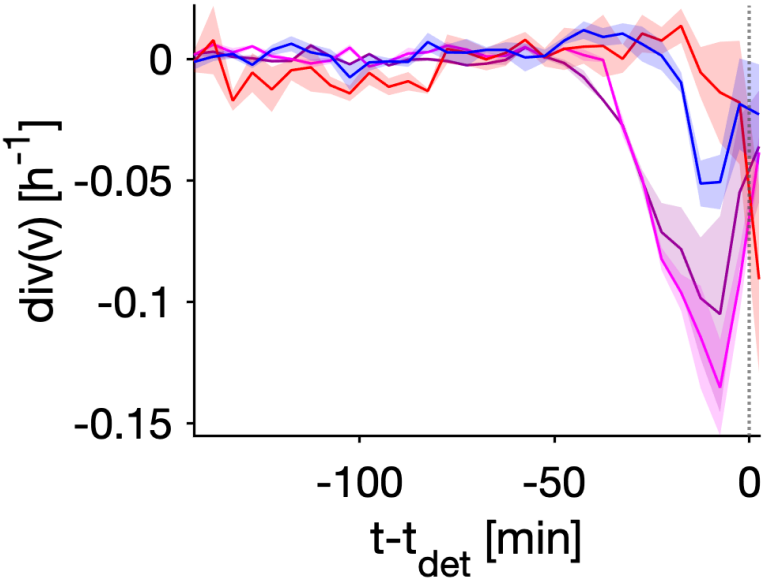

Figure 3.16: Formation profiles of individual domes under different conditions. *Divergence of velocity fields during dome formation plotted against time before dome formation (t - t_det, where t_det is the time of monolayer detachment/dome formation). The plot shows that divergence of velocity fields (analyzed by PIVLab) peaks in the negative direction just before dome formation, with lower peaks for blebbistatin conditions. Shaded areas denote ±1 SD (n=4 for control and PDMS, n=2 experiments for blebbistatin conditions). Red represents PDMS, blue represents control, pink represents blebbistatin 5 µM, and magenta represents blebbistatin 10 µM. These divergence values were calculated only from domes that formed before 96 hours (4 days) post-seeding. (Analysis performed by Dr. Stefano Villa.)*

3.5.2 Dome collapse dynamics reveal treatment-dependent behavior

By looking at the evolution of individual dome areas over time, we observe distinct collapse dynamics across conditions. As shown in Figure 3.17, for control cells (grown without treatment) and cells grown on PDMS, dome area increases steadily, reaches a peak, and then undergoes a sudden collapse. In contrast, domes formed under blebbistatin treatment exhibit a gradual relaxation into the monolayer rather than a sudden collapse.

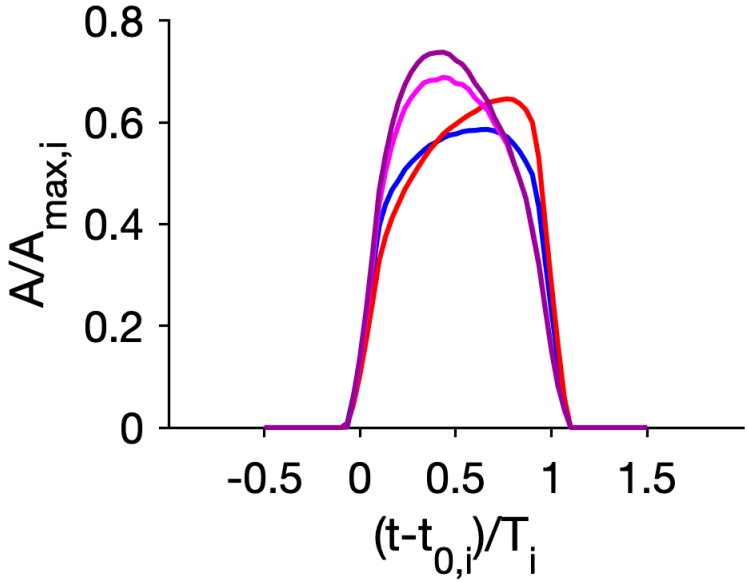

Figure 3.17: Average dome size evolution kinetics under different conditions. *Normalized dome area over normalized time. The Y-axis represents the area of each dome at a given time point normalized by its maximum area during its lifetime. The X-axis represents normalized time for each dome, starting from its formation. Control (blue) represents cells grown without treatment. Red represents cells grown on PDMS. Pink represents cells treated with 5 µM blebbistatin. Magenta represents cells treated with 10 µM blebbistatin. (Analysis performed by Dr. Stefano Villa.)*

3.6 Measurement of cell-substrate adhesion

To directly quantify how our treatments affect cell-substrate adhesion—a key parameter influencing dome formation—we attempted two complementary approaches.

3.6.1 Microfluidic shear assay is impeded by persistent air bubbles

When cells are grown on PDMS, dome formation is affected not only by cell motility, but also by cell-substrate adhesion (refer section 1.3).

Therefore, it is important to determine how our treatments with drugs influence cell-substrate adhesion. To investigate this, we tested two approaches:

1) Subject cells to fluid shear by injecting flow through a microfluidic chamber, then quantify the percentage of detached cells.
2) Subject cells to centrifugal shear using a custom-built spinning device, then quantify the percentage of detached cells.

Following up on the first approach, we fabricated PDMS microfluidic chambers with a single channel. The channel was coated with collagen and seeded with cells, which were allowed to adhere for two hours. After this adhesion period, cells were exposed to fluid flow at rates ranging from 22 to 30 mL/h. During shear application, brightfield images were acquired from 10 fields along the channel at 5-minute intervals over a total duration of 40 minutes.

The shear stress imposed by fluid flow on cells can be calculated using the Hagen-Poiseuille equation, assuming laminar flow conditions. However, these conditions were not met in our experiments due to the consistent and repeated occurrence of air bubbles within the channel. This made it impossible to reliably calculate the shear stress applied to the cells.

The following troubleshooting steps were attempted to resolve this issue:

- The chamber was washed with 0.2% Tween-20 surfactant in PBS before collagen coating to increase hydrophilicity, thereby allowing fluids to fill the channel more easily.
- A bubble trap (mp-bt Bubble Trap, Bartels Mikrotechnik) was connected between the syringe and the chamber inlet. This device uses negative pressure to separate air bubbles from the fluid.
- Silicone grease was applied to seal the points where tubing entered the PDMS device.
- The entire chip was submerged in water to prevent air from entering the device.

- All fluids were degassed using a vacuum chamber before introduction into the system.

Despite these measures, the problem of air bubbles persisted, as shown in Figure 3.19.

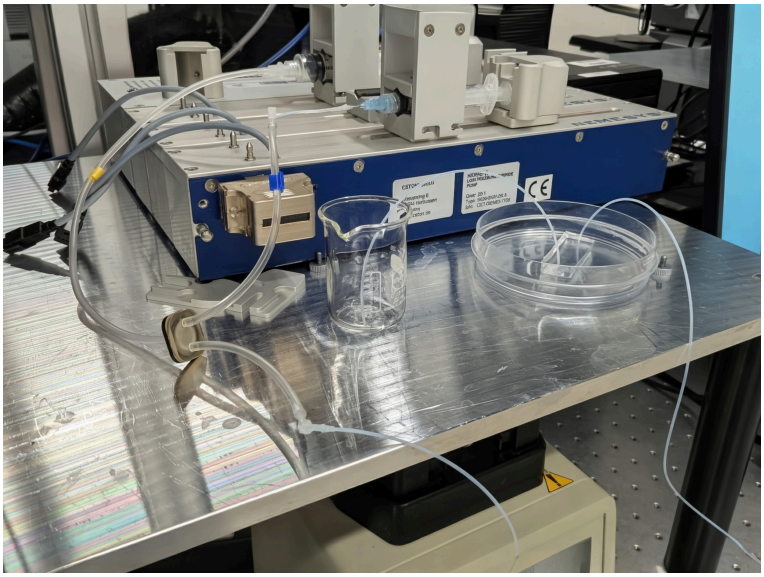

Figure 3.18: Setup of the microfluidic device*. The image shows the syringe mounted in the syringe pump, connected to the bubble trap, which is then connected to the microfluidic channel.*

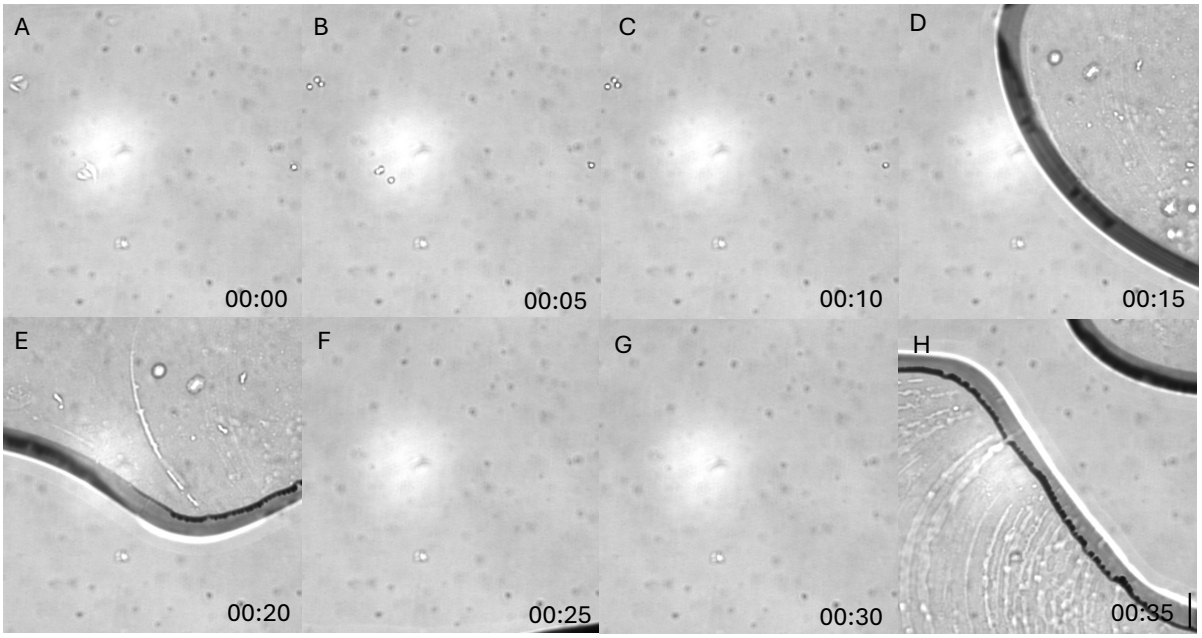

Figure 3.19: Timelapse of one field of view in the microfluidic chamber. *Images A-H show a series taken at 5-minute intervals from a single field of view as fluid was pumped through the chamber at 22 mL/h. Air bubbles can be seen forming and passing through the channel in images D, E, and H. Scale bar in F represents 200µm.*

3.6.2 Centrifugal adhesion assay quantifies cell adhesion under different substrates and treatments

The calculation of shear rate when using a spinning device is well characterized (García *et al.*, 1997). To implement this approach, we built a custom device (see Section 2.4.2). The shear stress experienced by cells can be calculated using established formulas and varies linearly with the radial distance from the center of the disk (García *et al.*, 1997). Representative snapshots from this assay are shown in Figure 3.20.

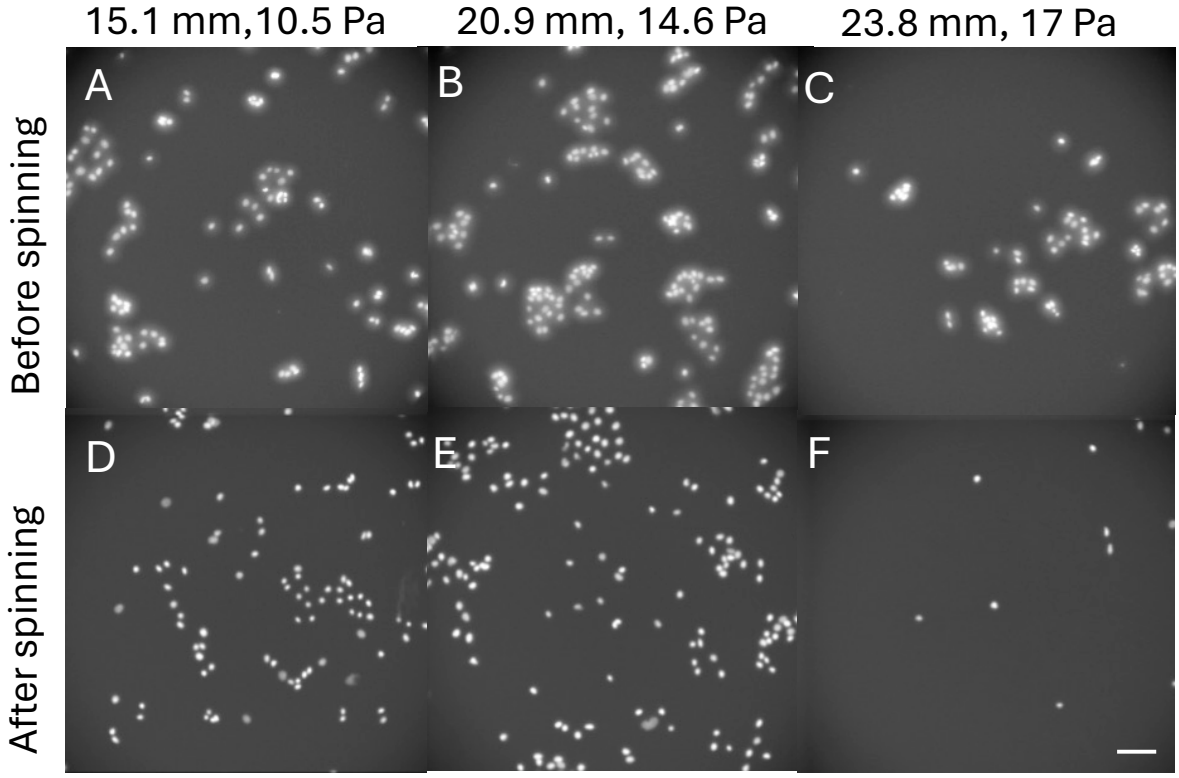

Figure 3.20: Decrease in cell density after centrifugal spinning*. Images shows the nuclei of cells (stained by Hoechst) before spinning (A, B, C) and after spinning (D, E, F). The distance from the center of rotation and the calculated shear stress are indicated at the top of each panel. Scale bar in F represents 100 µm. Please note that the field of view before and after spinning is not the same because of a positioning imprecision of the order of 150 µm.*

Using Hoechst staining to mark nuclei, we quantified cell detachment post-spinning by comparing images acquired from the same samples before and after spinning. We also assessed adhesion on fibronectin-coated substrates (40 µg/mL coating density), as this is the coating

condition used in Section 3.7. All other samples were grown on collagen-coated substrates (40µg/mL coating density). Quantification revealed that all conditions exhibited similar trends, showing an adhesion strength of about 16 Pa, with the exception of cells grown on PDMS. For PDMS, we observed complete detachment at shear stresses above 7 Pa, indicating that adhesion strength is lower than this threshold (Figure 3.21).

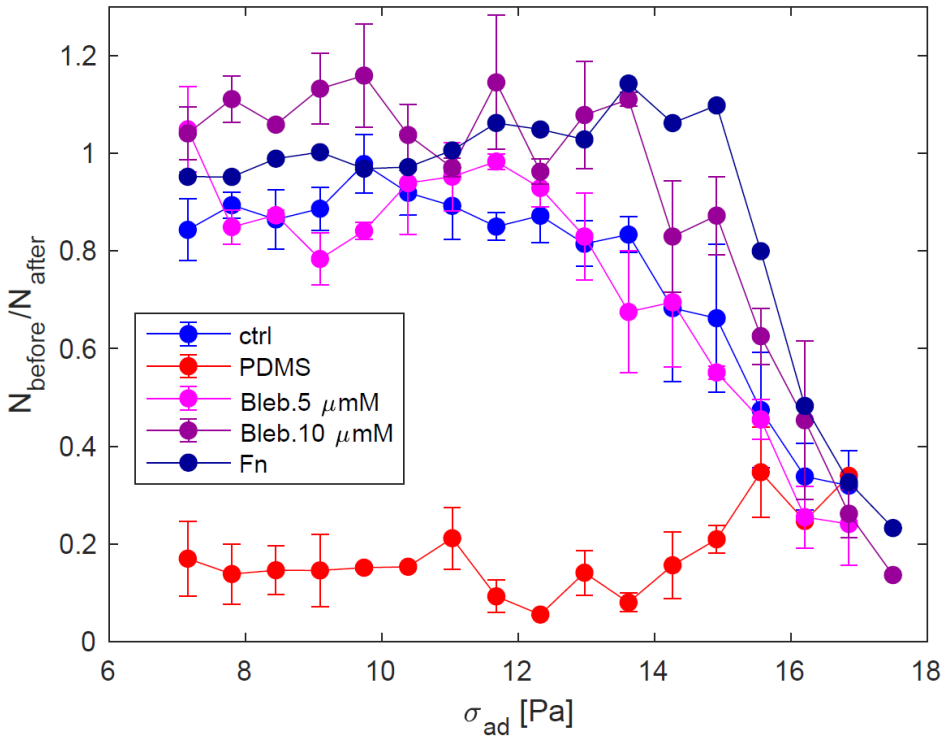

Figure 3.21: Fraction of adherent cells post-spinning normalized to pre-spinning cell number as a function of surface shear stress. *Error bars represent standard deviation evaluated over different biological samples for each condition: control (n=4), blebbistatin 5 µM and 10 µM (n=2), PDMS (n=2), and fibronectin 40 µg/mL (n=1) (Analysis performed by Dr. Stefano Villa).*

3.7 Micropatterned substrates induce cell stretching in domes

In a study by (Latorre *et al.*, 2018), fibronectin was micropatterned such that it was absent in circular areas, creating regions of low adhesion that imposed dome formation at specific locations. Under these conditions, in that study, cells on the dome experienced areal strains of up to 1000%. We suspected that this extreme stretching was due to the particular condition of domes being confined to form at specific locations. To test this, we prepared similarly

micropatterned surfaces. Using fluorescent fibronectin, we verified that our patterning was successful, as shown in Supplementary Figure 5.4.

Only when fibronectin was micropatterned, we were able to replicate their observations. As shown in Figure 3.22, the regions where yellow circles are positioned indicate expanded "superstretched" cells on micropatterned substrates. To quantify the cell area, we performed Voronoi tessellation on segmented nuclei and compared cell areas across conditions. Figure 3.23 shows that on micropatterned fibronectin, there are more cells with larger areas on the dome compared to cells outside the dome. In contrast, on uniform fibronectin layers, no such difference is observed. This supports our hypothesis that the extreme cell stretching reported by Latorre et al. is dependent on micropatterned adhesive islands rather than being an intrinsic property of dome formation. All our experiments reported in the other sections were carried out on uniform collagen coatings, so we do not expect to observe such superstretched states in our system.

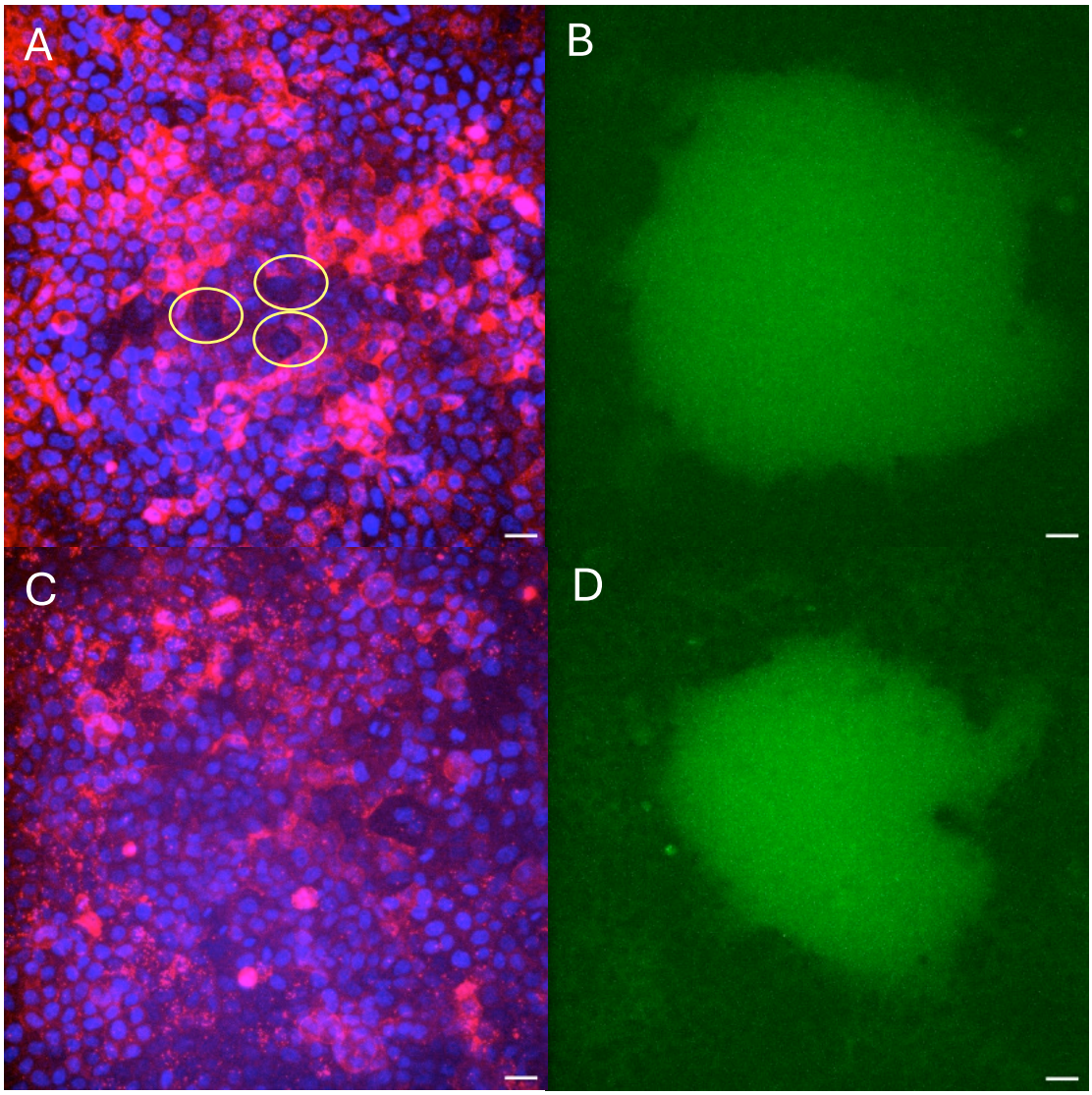

Figure 3.22: Visual comparison of domes grown on micropatterned versus uniform fibronectin. *(A) and (B) represent domes grown on patterned fibronectin and a uniform layer of 40 µg/mL fibronectin, respectively. In both cases, the left panel shows a maximum intensity projection of the actin channel (SiR Actin) in red and the nuclei channel (SPY595) in blue. The right panel shows the autofluorescence channel in green. In (A), yellow circles indicate regions where expanded "superstretched" cells are visible.*

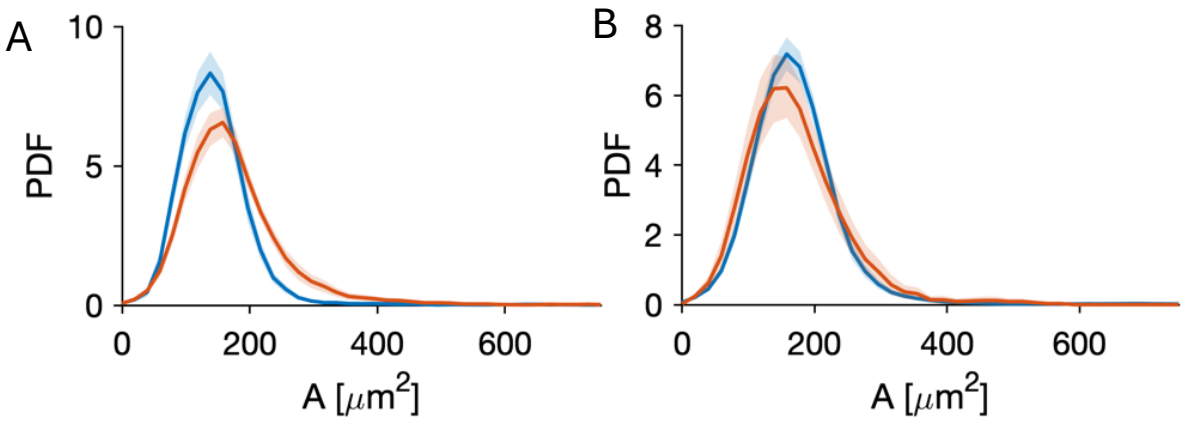

Figure 3.23: Cells on domes formed on micropatterned fibronectin show increased cell areas. *(A) and (B) represent the probability distribution functions of cell areas for domes grown on micropatterned and non-patterned fibronectin (40 µg/mL), respectively. (A) shows a clear shift in the peak of the probability distribution for cells on the dome compared to the adherent cells, indicating increased cell areas. This shift is absent in (B) for uniform fibronectin coatings. Orange represents cells on the dome, while pale blue represents adherent cells outside the dome, (n=8) (Analysis performed by Dr. Stefano Villa).*

4. Discussion

MDCKII domes exhibit a characteristic autofluorescence that fills the lumen and disappears upon dome collapse (Section 3.1.1). By analyzing the medium collected from beneath the cell monolayer, we confirmed that this fluorescent material is either a protein secreted by MDCKII cells in an apico-basal manner or an accumulation of ions beneath the monolayer (Figure 3.2). Furthermore, this autofluorescence cannot be attributed to the substrate, as it was consistently observed across multiple substrate types—including plastic, glass, and PDMS (Figure 3.9)—indicating that the signal is cell-derived and not an artifact of the culture surface. To distinguish between protein secretion and ion accumulation, future experiments using filters that retain proteins will determine whether this fluorescence arises from secreted factors. Additionally, we verified that this autofluorescence is not unique to our subline, as commercially obtained wild-type MDCKII cells showed similar patterns (Figure 3.3). Crucially, this intrinsic signal provides a non-invasive, label-free marker for the dome lumen, enabling us to track dome dynamics over long time periods without exogenous dyes.

To investigate the internal structure of domes, we performed second harmonic generation (SHG) imaging. Domes grown on collagen-coated substrates showed similar SHG signals to those grown without collagen (Figure 3.6). Since SHG detects non-centrosymmetric materials, including cross-linked collagen fibers (van Huizen et al., 2019), this suggests that if collagen is present within the dome, it is not in an organized, fibrillar form detectable by SHG, indicating that extensive remodeling into crosslinked fibers is not a feature of dome formation in our system.

Using third harmonic generation (THG), which detects lipid-water interfaces and, to a lesser extent, protein fiber-water interfaces (van Huizen et al., 2019), we observed a distinct fluorescent layer directly beneath domes (Figure 3.7). The signal was brighter around the dome edges, leading us to hypothesize that an actomyosin ring network might be present at the basal layer of cells at the dome periphery. However, subsequent visualization of actin filaments with SiR Actin (Figure 3.12) did not support this. The identity of this structure remains unclear and warrants further investigation, as it suggests the presence of an organized material beneath domes.

Using HGF and blebbistatin, we successfully increased and decreased cell dynamics, respectively. The HGF-treated samples, while showing increased motility, produced domes that were morphologically similar to the control (Figure 3.9) and were thus reserved for future studies. Importantly, blebbistatin-treated cells exhibited similar substrate adhesion to untreated controls (Figure 3.20), allowing us to attribute observed differences in dome behavior primarily to changes in contractility and motility rather than adhesion. In MDCKII cells, ion pumping activity should remain constant regardless of blebbistatin treatment, maintaining a consistent fluid flux. Despite this, dome parameters varied across conditions.

Blebbistatin-treated cells formed smaller domes that collapsed gradually rather than suddenly, with no change in adhesion strength (Figure 3.10D, 3.17). These cells lacked contractility due to myosin II inhibition, yet ion pumping—and thus fluid flux—remained unchanged. We propose that myosin II inhibition reduces the ability of cells surrounding the dome to resist the pressure generated by the rising dome. Consequently, the maximum stress they can withstand is lower, limiting dome growth and resulting in smaller dome sizes. The slow relaxation of domes observed in Figure 3.17 supports this interpretation: rather than collapsing suddenly, the dome reaches a maximum size and then slowly relaxes because the surrounding cells cannot sustain the stress.

Blebbistatin-treated conditions also showed a rapid increase in dome number, peaking around 80–100 hours before declining to a lower plateau (Figure 3.10E). This suggests a two-step process in blebbistatin-treated samples. Initially, the absence of actomyosin contractility prevents sudden collapse; domes simply relax back into the monolayer without rupturing, allowing repeated cycles of formation and relaxation. The lack of monolayer rupture implies that ions accumulated on the basal side are never released into the bulk, causing the osmotic pressure to increase continuously and driving the formation of more domes. Over time, however, reduced actomyosin tone may weaken cadherin-mediated cell-cell adhesion (Ladoux et al., 2010), eventually enabling fluid accumulation to overcome these weakened junctions and trigger collapse events similar to controls, albeit at lower pressures resulting in smaller domes. The shorter dome lifetime under blebbistatin treatment (Figure 3.10C) indicates rapid turnover of domes, leading to a lower plateau value for total monolayer detachment (Figure 3.10F). In control conditions, by contrast, fractures in monolayer integrity occur more consistently from the onset, allowing ions to leak back

into the bulk medium. Domes in controls also exhibit longer lifetimes (Figure 3.10C), contributing to the higher steady-state detachment ratio.

In contrast, cells grown on PDMS—which exhibit much lower substrate adhesion and higher motility—produced significantly larger domes while maintaining a collapse mechanism similar to controls (Figure 3.10D, 3.17). We propose that strong adhesion limits lateral dome expansion in other conditions by anchoring cells more firmly to the substrate. When this adhesive constraint is removed on PDMS, domes can expand to larger sizes before collapsing. Additionally, the higher motility observed on PDMS may facilitate the recruitment of cells into the growing dome structure, contributing to its expansion. Control and PDMS conditions reached similar plateau values for total monolayer detachment despite different timescales, suggesting that total detachment capacity is conserved in these two conditions.

Figures 3.12 through 3.15 demonstrate that actin and myosin actively participate in dome dynamics. Actin stress fibers confer contractility to cells (Kovaleva et al., 2025). Cells that collapse from the dome transiently lose these stress fibers, reducing their contractility and causing them to be pulled outward by surrounding cells. These cells reposition themselves once stress fibers reform. Blebbistatin treatment abolishes this recovery, confirming that actomyosin contractility drives the post-collapse reorganization observed in controls.

Finally, our micropatterning experiments revealed that the spatial distribution of adhesive proteins critically influences epithelial morphogenesis. When domes were confined to form on micropatterned fibronectin islands, cells exhibited superstretched areas (Figures 3.22 and 3.23), consistent with Latorre et al. (2018). Importantly, this extreme stretching was not observed on uniform coatings, suggesting that the superstretched state is a specific response to artificially imposed adhesive boundaries rather than an intrinsic feature of dome formation. Our experiments with uniform collagen coatings may therefore capture a more physiologically relevant mode of dome formation, where cells are not pre-patterned to detach at specific locations. This distinction underscores the crucial role of ECM organization in modulating epithelial responses to mechanical stress.

Together, these findings—dome kinetics under varied motility and adhesion, actin dynamics during collapse and recovery, and the influence of adhesive patterning—will

contribute to developing a comprehensive model explaining the interplay between cellular dynamics and mechanical stress in epithelial layers. Such a model is relevant to multiple physiological and pathological contexts, including alveolar expansion during breathing (Fredberg and Kamm, 2006), renal tubular fluid shear stress (Xu et al., 2020), intestinal peristalsis (Jing et al., 2020), and chronic inflammation or tumor progression (Jing et al., 2020; Khusnurrokhman and Wati, 2022). By building this model, we aim to advance understanding of how mechanical forces shape epithelial tissue behavior in health and disease, with implications for understanding epithelial morphogenesis, tissue mechanics, and biomaterial design.

Future Perspectives

Several avenues remain for future investigation. First, the origin of the autofluorescence signal requires further characterization. Using filters that retain proteins while allowing ions to pass will help determine whether the observed signal arises from secreted factors or ionic accumulation. Second, to better understand the role of cell dynamics at dome boundaries, a detailed analysis of cell motility at the periphery of micropatterned domes (as seen in Figure 3.22A) could reveal whether binning or holding down of cells occurs at dome boundaries. Tracking individual cells over time in these confined structures would provide insight into how spatial constraints influence cell positioning and collective behavior during dome formation. Third, the development of mathematical models incorporating ionic flux, cell adhesion, and cell motility would provide a framework for predicting the time evolution of dome number and area across conditions. Such models are already being developed by Dr. Stefano Villa using the data collected in this study. Fourth, to test our hypothesis that the blebbistatin-induced peak in dome number followed by a lower plateau reflects a two-step process, future experiments could employ different drugs that modulate motility and contractility, or add blebbistatin at later time points to assess whether the timing of the transition is altered. Finally, the identity of the THG signal observed beneath domes remains unknown; combining THG with specific molecular probes for possible proteins could help identify this material and elucidate its role in dome formation. These future directions will not only deepen our mechanistic understanding of dome dynamics but also inform broader principles of epithelial tissue mechanics.

5. Appendix

5.1 Collagen coating conditions do not substantially alter cell dynamics

To visually inspect our collagen coating under the microscope, we used FITC-tagged collagen in some experiments at a concentration of 4 µg/mL. To ensure that our collagen coating protocol did not inadvertently affect cell behavior, we compared multiple coating conditions. The following conditions were tested to check if there was a difference in the cell dynamics:

Control: Cells plated directly on the Petri dish
Collagen FITC 40 µg/mL
Collagen FITC 4 µg/mL
Collagen from calf skin 4 µg/mL
Collagen from calf skin 40 µg/mL
Collagen FITC dissolved in water 4 µg/mL (since collagen coated at neutral pH shows higher crosslinking (Chuang *et al.*, 2018) we wanted to test this condition as well)

As shown in Figure 5.1, cell dynamics were similar across all conditions, with one exception: the v_{rms} of Collagen FITC conditions showed slightly lower values over time compared to all other conditions, but it lies within the usually observed inter-sample variability (around 1µm/h).

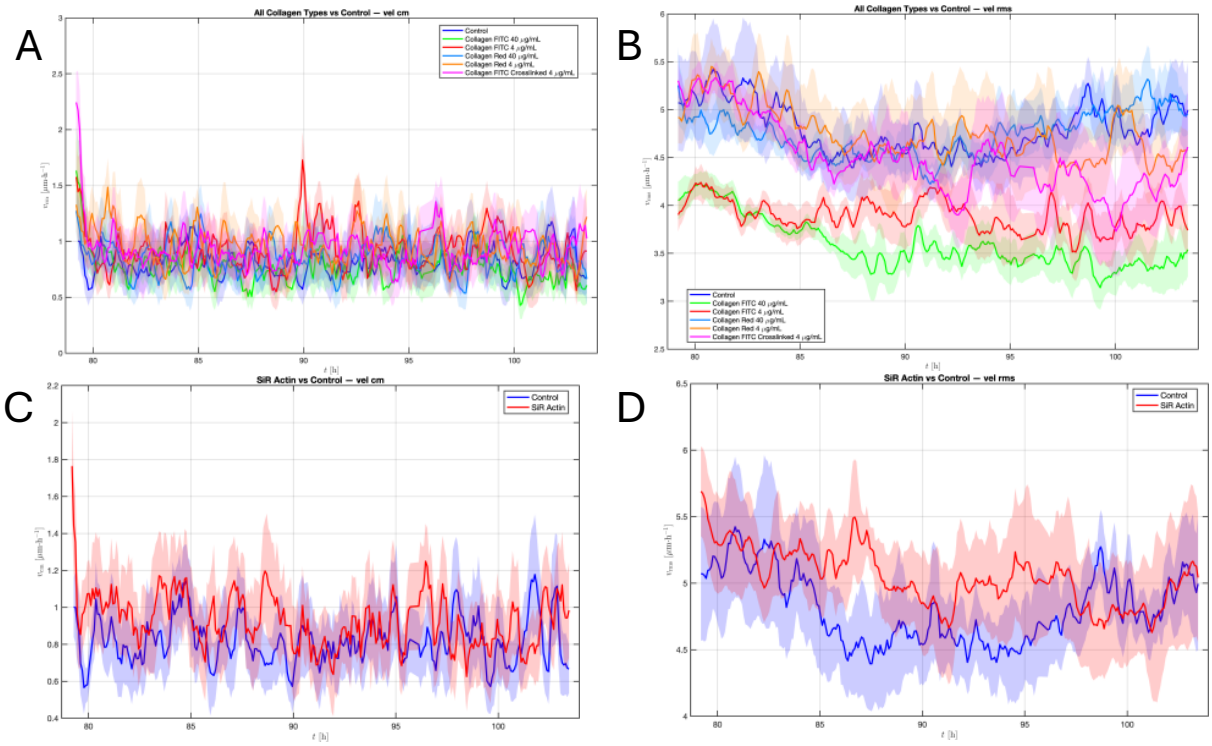

Supplementary figure 5.1: Dynamics on different substrates. *(A) and (C) show v_{cm} plots. (B) and (D) show v_{rms} plots. Color code: Control no coating (blue), Collagen FITC 40 µg/mL (bright green), Collagen FITC 4 µg/mL (red), Collagen from calf skin 40 µg/mL (sky blue), Collagen from calf skin 4 µg/mL (orange), Collagen FITC dissolved in water 4 µg/mL (magenta). n=1 experiment. T=0 represents the time of cell seeding. Solid lines represents the mean; shaded area denotes ±1 SD. (Code for analysis written by Dr. Stefano Villa).*

5.2 DMSO solvent control shows no effect on cell motility

Since we dissolve blebbistatin in DMSO, we performed a control experiment to check cell dynamics with and without 1 µL DMSO—the volume of solvent used for the highest concentration of blebbistatin (10 µM) in our experiments. As shown in Figure 5.2, both control and DMSO-treated conditions exhibited similar trends in cell dynamics. As blebbistatin is dissolved in DMSO, we verified that the solvent alone does not alter cell

dynamics.

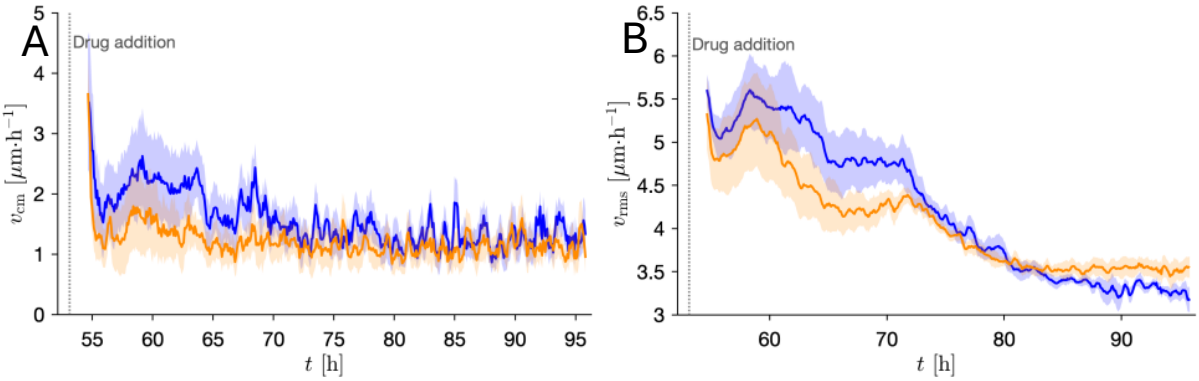

***Supplementary figure 5.2: Dynamics of control and DMSO conditions**. (A) represents v_{cm} evolution over time. (B) represents v_{rms} evolution over time. Both control and DMSO show similar trends. Color code: Control (blue), DMSO 1ul (ochre yellow). n=3. T=0 represents the time of cell seeding. Solid lines represents the mean; shaded area denotes ±1 SD. (Code for analysis written by Dr. Stefano Villa).*

5.3 HGF dose-response establishes optimal concentrations for motility modulation

To determine the optimal HGF concentrations that would produce clear differences in cell velocity, we tested a wide range: 0, 2.5, 5, 10, 20, 40, and 80 ng/mL. Results are shown in Figure 5.3. We chose HGF 40 and 80ng/ml for further experiments as they showed a differentiable increase in v_{rms}.

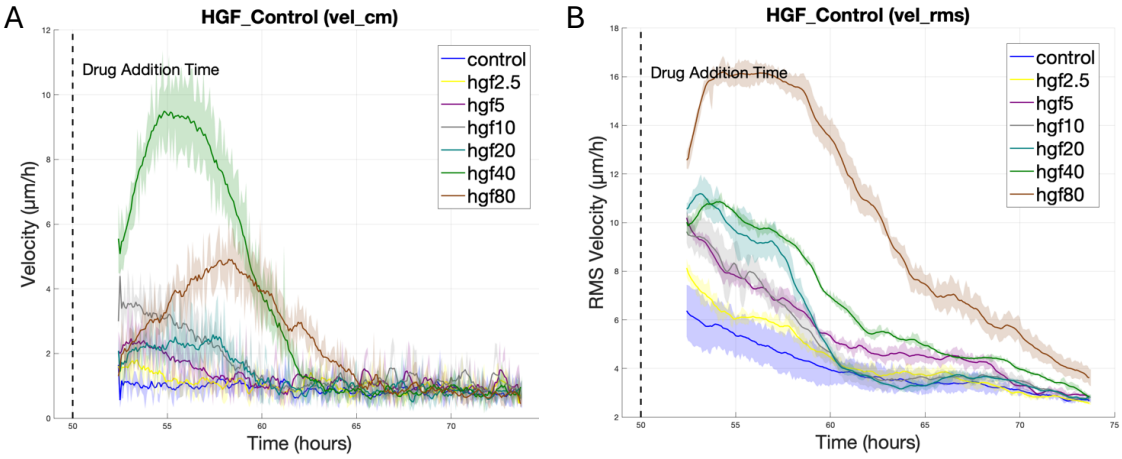

***Supplementary figure 5.3: Collective dynamics of MDCKII cells under different concentrations of HGF.** The figure shows how v_{cm} and v_{rms} change over time when HGF at concentrations of 0, 2.5, 5, 10, 20, 40, and 80 ng/mL were added. T=0 represents*

the time of cell seeding. Solid lines represents the mean; shaded area denotes ±1 SD. (Code for analysis written by Dr. Stefano Villa).

5.4 Fluorescent fibronectin confirms successful micropatterning

To verify that our micropatterning of fibronectin on substrates was successful, we used fluorescent fibronectin for visualization. Stamps of 100 µm diameter were used as stated in section 2.2.4 for micropatterning, which proved successful. The micropattern can be observed in Figure 5.4.

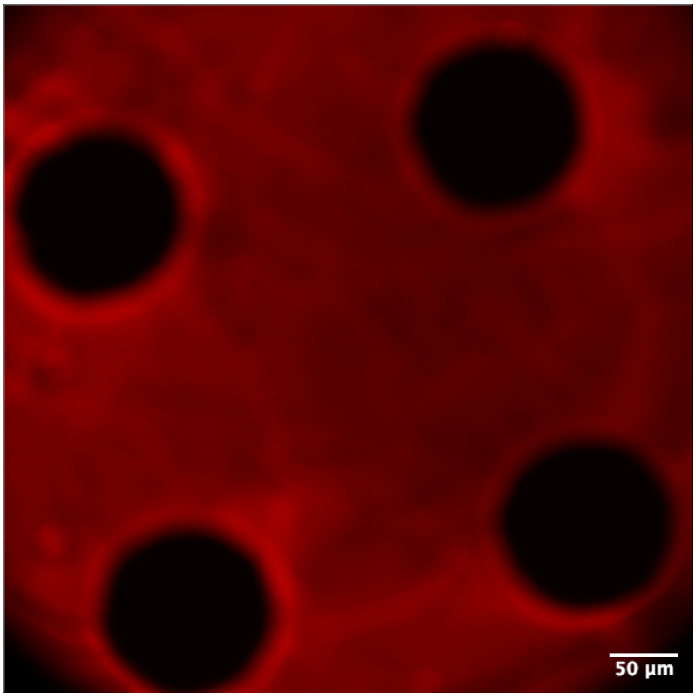

Supplementary figure 5.4: *Fibronectin micropatterning. The image shows fluorescent fibronectin (40 µg/mL coating concentration) imprinted on the PDMS surface, visualized using epifluorescence microscopy.*

5.5 Blebbistatin does not increase cell death

To assess whether blebbistatin treatment increases cell death, we performed a death assay as described in Section 2.3.1.1. As shown in Supplementary Figure 5.6, no clear increase in cell death was observed upon drug treatment, and no consistent trends emerged across conditions.

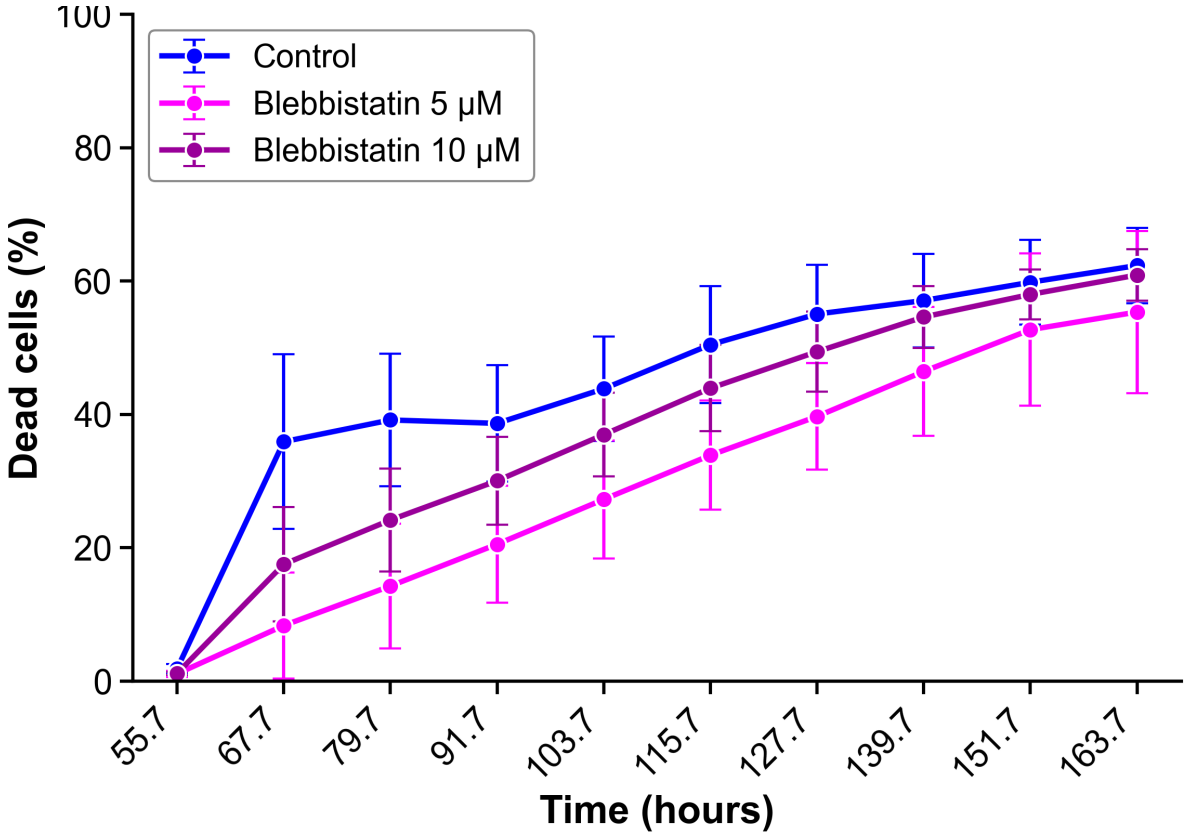

Supplementary figure 5.6: Cell death assay. The figure represents the percentage of dead cells over time following blebbistatin treatment. *Solid lines represents the mean;error bars denotes ±1 SD. T=0 represents the time of cell seeding.*

In this assay, EthD-1 staining marks dead cells. To visually interpret these results, we overlapped the EthD-1 channel with brightfield images in Supplementary Figure 5.7. This visualization reveals that most dead cells observed by this method are extruded from the monolayer. Since these cells are no longer part of the intact monolayer, they do not affect the dynamics within it and are replaced by duplication of other cells. Therefore, although Supplementary Figure 5.6 shows dead cell percentages reaching up to 60% in some conditions, this does not indicate that 60% of cells within the monolayer are dead. Rather, it reflects the accumulation of extruded cells over time.

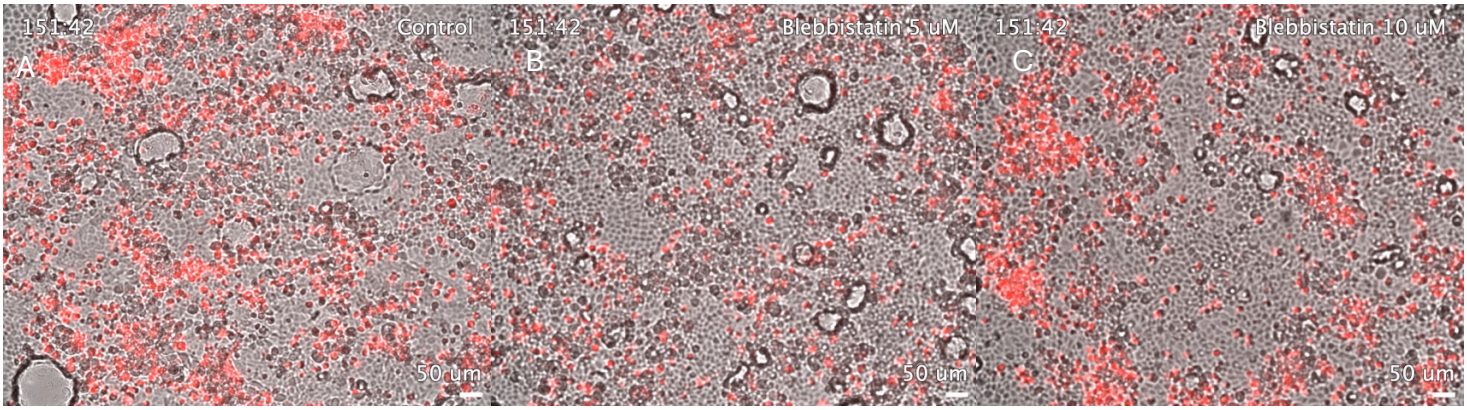

Supplementary Figure 5.7: Visual representation of dead cells using EthD-1 staining. *(A) Control, (B) blebbistatin 5 µM, and (C) blebbistatin 10 µM. Brightfield channel is shown in gray, and EthD-1 staining is shown in red. Images are representative and do not encompass all data acquired. Scale bar represents 50 µm.*

5.6 Attempt to generate H2B-eGFP and mCherry stable cell lines

Several attempts were made to transfect MDCKII cells with H2B-eGFP and H2B-mCherry plasmids using the calcium phosphate transfection method(see section 2.5). By Day 5 post-transfection, successful transfection was observed in approximately 10–20% of cells, as assessed by fluorescence microscopy (Supplementary Figure 5.8). Following this, we applied G418 selection at 0.2 mg/mL, a concentration determined from a preliminary kill curve. However, by Day 10, most cells had died.

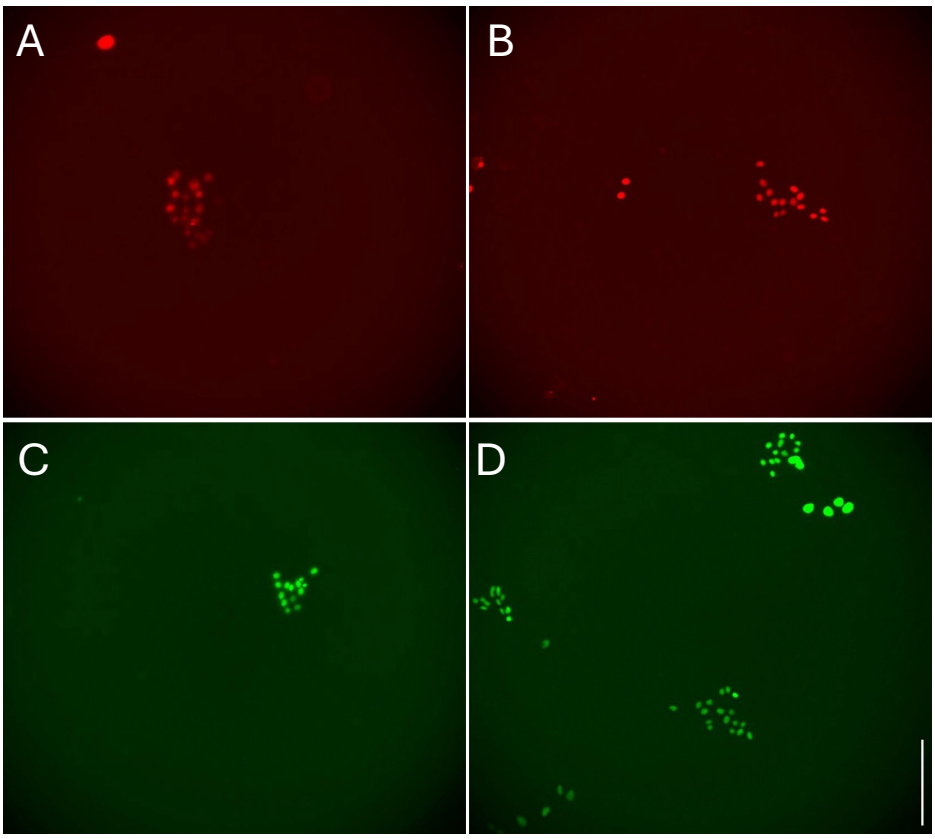

Supplementary Figure 5.8: Successful nuclear fluorescence observed on day 5 post-transfection. *Both mCherry (A, B) and eGFP (C, D) appear to be expressed and localized to the nuclei, as observed in their respective fluorescence channels. Scale bar in D represents 200 µm.*

The failure to establish stable lines is likely due to low rates of genomic integration with calcium phosphate transfection, a known limitation of this method. Future attempts will focus on increasing sample size and passaging cells for multiple generations to select for stable integrants.

5.7 Verification of rotation speed of custom spinning device using a high-speed camera

A high-speed camera was used (see Section 2.6.5) to verify whether the rotation speed of our custom adhesion assay device matched the nominal RPM displayed on the magnetic stirrer. As shown in Supplementary Figure 5.9, the nominal RPM closely matched the measured rotational frequency for 500 RPM, 750 RPM, and 1000 RPM. However, at higher speeds such as 1400 RPM, the measured frequency deviated from the nominal value. Since all experiments in this study used a rotation speed of 1000 RPM, we confirm that our device

operated at the intended speed for all adhesion measurements.

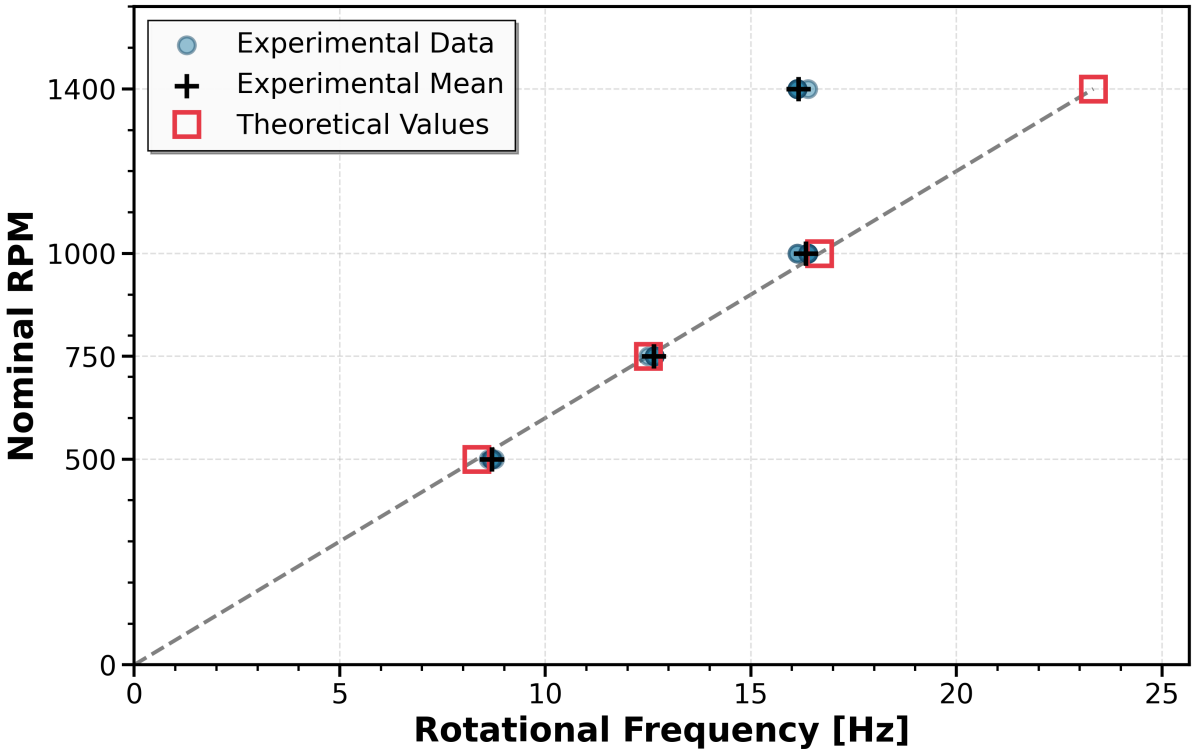

Supplementary Figure 5.9: Verification of rotation speed. *Nominal RPM plotted against measured rotational frequency. The theoretical line represents perfect correspondence between nominal and measured values. Measurements were averaged over n=10 time periods for each speed tested.*

6. References

Atarashi, K, Suda, W, Luo, C, Kawaguchi, T, Motoo, I, Narushima, S, Kiguchi, Y, Yasuma, K, Watanabe, E, Tanoue, T, *et al.* (2017). Ectopic colonization of oral bacteria in the intestine drives TH1 cell induction and inflammation. Science 358, 359–365.

Brightling, CE, Gupta, S, Gonem, S, and Siddiqui, S (2012). Lung damage and airway remodelling in severe asthma. Clin Exp Allergy 42, 638–649.

Brückner, BR, and Janshoff, A (2018). Importance of integrity of cell-cell junctions for the mechanics of confluent MDCK II cells. Sci Rep 8, 14117.

Candiello, J, Balasubramani, M, Schreiber, EM, Cole, GJ, Mayer, U, Halfter, W, and Lin, H (2007). Biomechanical properties of native basement membranes. FEBS J 274, 2897–2908.

Cartwright, JE, Tse, WK, and Whitley, GStJ (2002). Hepatocyte Growth Factor Induced Human Trophoblast Motility Involves Phosphatidylinositol-3-Kinase, Mitogen-Activated Protein Kinase, and Inducible Nitric Oxide Synthase. Exp Cell Res 279, 219–226.

Charras, GT, Hu, C-K, Coughlin, M, and Mitchison, TJ (2006). Reassembly of contractile actin cortex in cell blebs. J Cell Biol 175, 477–490.

Chiquet, M, Puri, EC, and Turner, DC (1979). Fibronectin mediates attachment of chicken myoblasts to a gelatin-coated substratum. J Biol Chem 254, 5475–5482.

Choudhury, MI, Li, Y, Mistriotis, P, Vasconcelos, ACN, Dixon, EE, Yang, J, Benson, M, Maity, D, Walker, R, Martin, L, *et al.* (2022). Kidney epithelial cells are active mechano-biological fluid pumps. Nat Commun 13, 2317.

Chuang, C-H, Lin, R-Z, Melero-Martin, JM, and Chen, Y-C (2018). Comparison of covalently and physically cross-linked collagen hydrogels on mediating vascular network formation for engineering adipose tissue. Artif Cells Nanomedicine Biotechnol 46, S434–S447.

Clemente-Suárez, VJ, Martín-Rodríguez, A, Redondo-Flórez, L, Villanueva-Tobaldo, CV, Yáñez-Sepúlveda, R, and Tornero-Aguilera, JF (2023). Epithelial Transport in Disease: An Overview of Pathophysiology and Treatment. Cells 12, 2455.

Cotovio, J, Roguet, R, Cambar, J, Rougier, A, and Dossou, KG (1993). Quantification of dome formation by image analysis in LLC-PK1 renal cells: A sensitive method for the assessment of in vitro nephrotoxicity. J Tissue Cult Methods 15, 117–122.

Eichenberger-Glinz, S (1979). Intercellular junctions during development and in tissue cultures ofDrosophila melanogaster: An electron-microscopic study. Wilhelm Rouxs Arch Dev Biol 186, 333–349.

Fu, J, Su, X, Li, Z, Deng, L, Liu, X, Feng, X, and Peng, J (2021). HGF/c-MET pathway in cancer: from molecular characterization to clinical evidence. Oncogene 40, 4625–4651.

García, AJ, Ducheyne, P, and Boettiger, D (1997). Quantification of cell adhesion using a spinning disc device and application to surface-reactive materials. Biomaterials 18, 1091–1098.

Gelse, K (2003). Collagens—structure, function, and biosynthesis. Adv Drug Deliv Rev 55, 1531–1546.

Guo, L, Wang, L, Yang, R, Feng, R, Li, Z, Zhou, X, Dong, Z, Ghartey-Kwansah, G, Xu, M, Nishi, M, *et al.* (2017). Optimizing conditions for calcium phosphate mediated transient transfection. Saudi J Biol Sci 24, 622–629.

Höök, M, Rubin, K, Oldberg, Å, Öbrink, B, and Vaheri, A (1977). Cold-insoluble globulin mediates the adhesion of rat liver cells to plastic petri dishes. Biochem Biophys Res Commun 79, 726–733.

Hotulainen, P, and Lappalainen, P (2006). Stress fibers are generated by two distinct actin assembly mechanisms in motile cells. J Cell Biol 173, 383–394.

Hsieh, C-H, Kuo, W-T, Huang, Y-C, and Huang, Y-Y (2011). High-efficiency cell seeding method by relatively hydrophobic culture strategy. J Biomed Mater Res B Appl Biomater 98B.

van Huizen, LMG, Kuzmin, NV, Barbé, E, van der Velde, S, te Velde, EA, and Groot, ML (2019). Second and third harmonic generation microscopy visualizes key structural components in fresh unprocessed healthy human breast tissue. J Biophotonics 12, e201800297.

Ishida-Ishihara, S, Akiyama, M, Furusawa, K, Naguro, I, Ryuno, H, Sushida, T, Ishihara, S, and Haga, H (2020). Osmotic gradients induce stable dome morphogenesis on extracellular matrix. J Cell Sci 133, jcs243865.

Jing, B, Wang, Z, Zhang, C, deng, Q, Wei, J, Luo, Y, Li, J, and Du, Y (2020). Establishment and Application of Peristaltic Human Gut-Vessel Microsystem for Studying Host–Microbial Interaction. Front Bioeng Biotechnol 8, 272.

Khusnurrokhman, G, and Wati, FF (2022). Tumor-promoting inflammation in lung cancer: A literature review. Ann Med Surg 79.

Kovács, M, Tóth, J, Hetényi, C, Málnási-Csizmadia, A, and Sellers, JR (2004). Mechanism of blebbistatin inhibition of myosin II. J Biol Chem 279, 35557–35563.

Kovaleva, A, Solomatina, E, Tlegenova, M, Saidova, A, and Vorobjev, IA (2025). How Actin Polymerization and Myosin II Activity Regulate Focal Adhesion Dynamics in Motile Cells. Int J Mol Sci 26, 7701.

Kozyrina, AN, Piskova, T, and Di Russo, J (2020). Mechanobiology of Epithelia From the Perspective of Extracellular Matrix Heterogeneity. Front Bioeng Biotechnol 8, 596599.

Kumar, S, Maxwell, IZ, Heisterkamp, A, Polte, TR, Lele, TP, Salanga, M, Mazur, E, and Ingber, DE (2006). Viscoelastic Retraction of Single Living Stress Fibers and Its Impact on Cell Shape, Cytoskeletal Organization, and Extracellular Matrix Mechanics. Biophys J 90, 3762–3773.

Ladoux, B, Anon, E, Lambert, M, Rabodzey, A, Hersen, P, Buguin, A, Silberzan, P, and Mège, R-M (2010). Strength Dependence of Cadherin-Mediated Adhesions. Biophys J 98, 534–542.

Latorre, E, Kale, S, Casares, L, Gómez-González, M, Uroz, M, Valon, L, Nair, RV, Garreta, E, Montserrat, N, del Campo, A, *et al.* (2018). Active superelasticity in three-dimensional epithelia of controlled shape. Nature 563, 203–208.

Lever, JE (1979a). Inducers of mammalian cell differentiation stimulate dome formation in a differentiated kidney epithelial cell line (MDCK). Proc Natl Acad Sci 76.

Lever, JE (1979b). Regulation of dome formation in differentiated epithelial cell cultures. J Supramol Struct 12, 259–272.

Madin, SH, and DarbyJr, NB (1958). Established Kidney Cell Lines of Normal Adult Bovine and Ovine Origin.∗. Proc Soc Exp Biol Med 98, 574–576.

Müller, HA, and Wieschaus, E (1996). armadillo, bazooka, and stardust are critical for early stages in formation of the zonula adherens and maintenance of the polarized blastoderm epithelium in Drosophila. J Cell Biol 134, 149–163.

Nasufovic, V, Kompa, J, Lindamood, HL, Blümke, M, Koch, B, Le-vario-Diaz, V, Weber, K, Maager, M, Cavalcanti-Adam, EA, Vitriol, EA, *et al.* (2025). SiR-XActin: A fluorescent probe for imaging actin dynamics in live cells. bioRxiv, 2025.02.04.636537.

Patrito, N, McCague, C, Norton, PR, and Petersen, NO (2007). Spatially Controlled Cell Adhesion via Micropatterned Surface Modification of Poly(dimethylsiloxane). Langmuir 23, 715–719.

Saw, TB, Doostmohammadi, A, Nier, V, Kocgozlu, L, Thampi, S, Toyama, Y, Marcq, P, Lim, CT, Yeomans, JM, and Ladoux, B (2017). Topological defects in epithelia govern cell death and extrusion. Nature 544, 212–216.

Seifter, JL, and Chang, H-Y (2017). Extracellular Acid-Base Balance and Ion Transport Between Body Fluid Compartments. Physiology 32, 367–379.

Shiel, MJ, and Caplan, MJ (1995). Developmental regulation of membrane protein sorting in Drosophila embryos. Am J Physiol-Cell Physiol 269, C207–C216.

Siddique, A, Meckel, T, Stark, RW, and Narayan, S (2017). Improved cell adhesion under shear stress in PDMS microfluidic devices. Colloids Surf B Biointerfaces 150, 456–464.

Spring, KR (2011). Mechanism of Fluid Transport by Epithelia. In: Comprehensive Physiology, John Wiley & Sons, Ltd, 195–207.

Sugahara, K, Caldwell, JH, and Mason, RJ (1984). Electrical currents flow out of domes formed by cultured epithelial cells. J Cell Biol 99, 1541–1544.

Thielicke, W. (2014). The flapping flight of birds: Analysis and application. PhD thesis, University ofGroningen.

Tschumperlin, DJ, and Margulies, SS (1999). Alveolar epithelial surface area-volume relationship in isolated rat lungs. J Appl Physiol Bethesda Md 1985 86, 2026–2033.

Vaheri, A, Ruoslahti, E, Westermark, B, and Ponten, J (1976). A common cell-type specific surface antigen in cultured human glial cells and fibroblasts: loss in malignant cells. J Exp Med 143, 64–72.

Winter, SE, Keestra, AM, Tsolis, RM, and Bäumler, AJ (2010). The Blessings and Curses of Intestinal Inflammation. Cell Host Microbe 8, 36–43.

Wirl, G, Hermann, M, Ekblom, P, and Fässler, R (1995). Mammary epithelial cell differentiation in vitro is regulated by an interplay of egf action and tenascin-c downregulation. J Cell Sci 108, 2445–2456.

.